Title: Control of flight responses by a non-canonical corticolimbic pathway.

Authors: Chandrashekhar D. Borkar[1,2], Xin Fu[3], Claire E. Stelly[1,2], Maria Dorofeikova[1,2], Quan-Son Eric Le[2,3], Rithvik Vutukuri[2,3], Catherine Vo[2,3], Samhita Basavanhalli[2,3], Anh Duong[2,3], Erin Bean[2,3], Alexis Resendez[1,2], Jones G. Parker[4], Jeffrey G. Tasker[5], Jonathan P. Fadok[1,2]*

Affiliations:

[1] Department of Psychology, Tulane University, New Orleans, LA 70118, USA

[2] Tulane Brain Institute, Tulane University, New Orleans, LA 70118, USA

[3] Neuroscience Program, Tulane University, New Orleans, LA 70118, USA

[4] Department of Neuroscience, Feinberg School of Medicine, Northwestern University, Chicago, IL 60611, USA

[5] Department of Cell and Molecular Biology, Tulane University, New Orleans, LA 70118, USA

*Corresponding author: Jonathan P. Fadok

Tulane Brain Institute, 6823 St. Charles Ave., New Orleans, LA 70118-5698, USA.

E-mail address: jfadok@tulane.edu.

ABSTRACT

Survival requires the selection of appropriate behaviour in response to threats, and dysregulated defensive reactions are associated with psychiatric illnesses such as posttraumatic stress and panic disorder.[1] Threat-induced behaviour, including panic-like flight, is controlled by neuronal circuits in the central amygdala (CeA)[2]; however, the source of neuronal excitation to the CeA that contributes to these high-intensity defensive responses is unknown. Here we used a combination of neuroanatomical mapping, *in-vivo* calcium imaging, functional manipulations, and slice physiology to characterize a

previously unknown projection from the dorsal peduncular (DP) prefrontal cortex to the CeA. DP-to-CeA neurons are glutamatergic and specifically target the medial CeA. Using a behavioural paradigm that elicits both freezing and flight, we found that CeA-projecting DP neurons are activated by high-intensity threats in a context-dependent manner. Functional manipulations revealed that the DP-to-CeA pathway is necessary for both avoidance behaviour and flight. Furthermore, we found that DP projections preferentially target distinct medial CeA neuronal populations linked to flight. These results are the first demonstration that the prefrontal cortex exerts direct, top-down control of the CeA and elucidate a non-canonical pathway regulating panic-like fear responses.

In the face of threat, organisms display a continuum of defensive behaviours and flexibly shift between defensive strategies.[3,4] Selecting the appropriate action for survival depends on the proximity and intensity of the threat and the context of the encounter.[5,6] Moreover, exaggerated responses to perceived threats have been associated with anxiety, post-traumatic stress and panic disorders, and phobias.[1,7,8,9] Abnormal patterns of activation in the prefrontal cortex (PFC) are associated with these mental illnesses, and bidirectional projections between the medial PFC (mPFC) and basolateral amygdala are part of a canonical pathway that has been extensively studied in the acquisition and expression of learned fear measured with freezing.[10–14] Previous studies have shown that animals exhibit behavioural scaling to favour flight over freezing in response to a high-intensity threat, and conditional freeze-to-flight shifting is regulated by distinct and mutually inhibitory local circuit motifs in the CeA.[2,15,16] Whether the cortex exerts top-down control of these behavioural shifts is not fully understood. Interestingly, the mPFC also projects to the CeA,[17] raising the possibility that a direct pathway from mPFC to CeA could influence defensive action selection. However, this pathway has never been defined neuroanatomically, and its role in regulating defensive behaviour is unknown.

53 **Direct mPFC projections to medial CeA**

54 To determine which subdivision of the mPFC projects to the CeA, we injected fluorescent,
55 retrogradely trafficked latex microspheres into the CeA (**Fig. 1A, B**). We observed sparse
56 projections from both the prelimbic (PL) and infralimbic (IL) cortices. However, a significantly
57 greater number of CeA projectors were located in the dorsal peduncular nucleus (DP; **Fig. 1C, D;**
58 **Fig. S1A**), a region of the mPFC recently linked to physiological and behavioural responses to
59 stress.[18]

60

61 The mPFC regulates cognition, motivation, and emotion via distinct glutamatergic projections to
62 cortical and subcortical regions.[19] The vesicular glutamate transporter (Vglut) 1 is used to label
63 most excitatory cortical neurons, yet the DP is enriched in both the Vglut1 and Vglut2 isoforms,
64 which define different populations of projection neurons.[20] To characterize the DP-to-CeA
65 pathway more precisely, we injected a viral vector into the DP of Vglut1- or Vglut2-Cre mice (**Fig.**
66 **1E-G**). We found that the Vglut1 fibre density within the CeA was significantly higher than that of
67 Vglut2 (**Fig. 1H-J**). Notably, these fibres were most abundant in the medial subdivision of the CeA
68 (CeM), as compared to the lateral (CeL) or capsular (CeC) subdivisions (**Fig. 1J**). Therefore,
69 Vglut1-expressing DP neurons are anatomically positioned to influence fear via direct projections
70 to the primary amygdalar output centre that controls the expression of defensive behaviour.

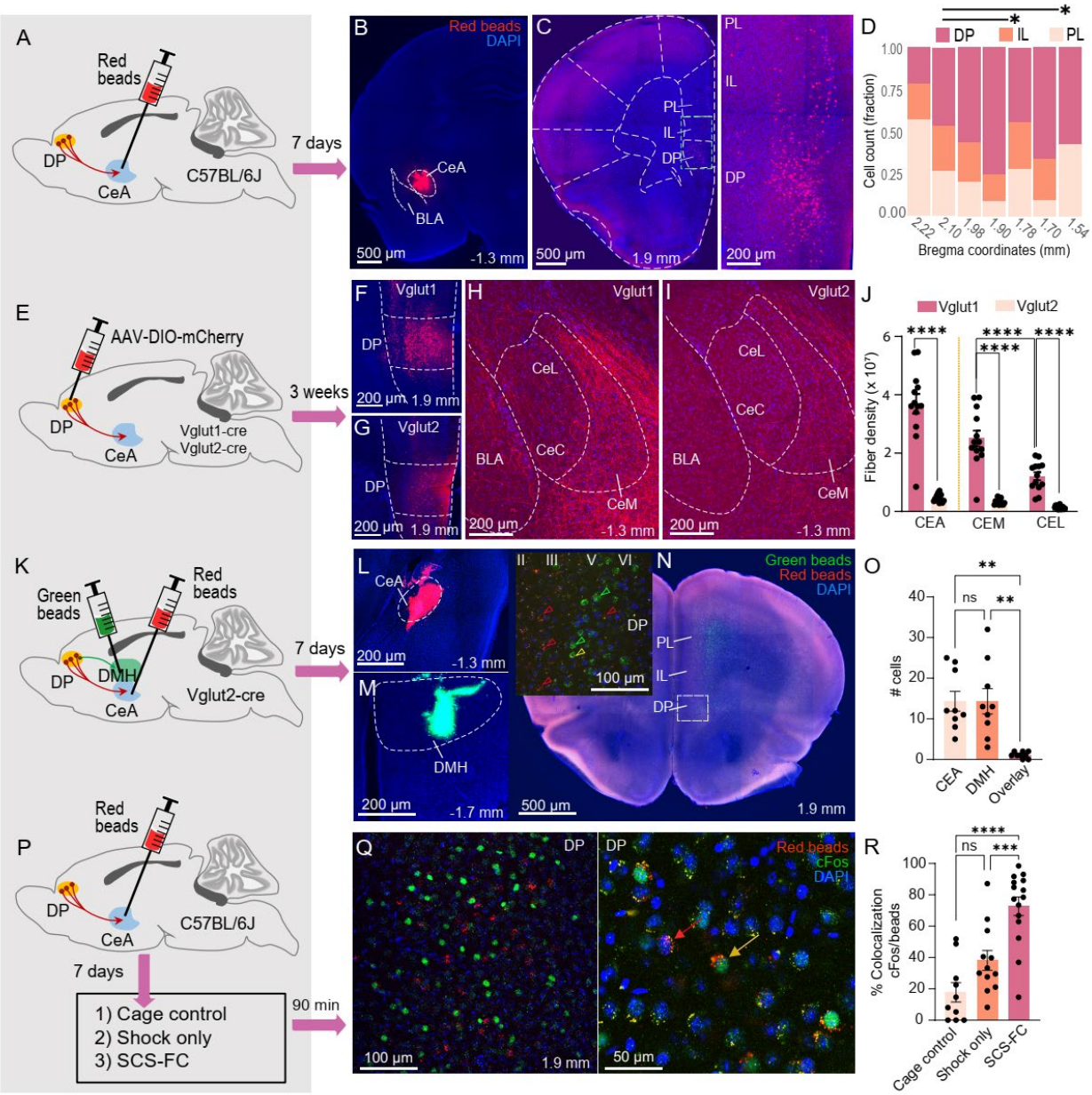

Figure 1. Neuroanatomical characterization of the DP-to-CeA pathway.

A, Schematic diagram showing retrograde tracing strategy.

B, Histology image showing injection site of red beads in the CeA.

C, Histology images of red retro-beads+ neurons in the DP (at 5x *(left)* and 10x *(right)* magnification).

D, Distribution of CeA-projecting neurons from mPFC subregions (One-way ANOVA, $F_{(2,15)}$ = 5.51, p = 0.016; Bonferroni's post-hoc test, *p<0.05 vs DP; N = 6; 5-7 sections/mouse). DP, dorsal peduncular cortex; IL, infralimbic cortex; PL, prelimbic cortex.

E, Strategy used to trace glutamatergic terminals in the CeA.

F, Representative image of DP targeting in Vglut1-Cre mice.

G, Representative image of DP targeting in Vglut2-Cre mice.

H, Representative expression of mCherry+ terminals in the CeA of a VGlut1-Cre mouse.

I, Representative expression of mCherry+ terminals in the CeA of a VGlut2-Cre mouse.

J, Integrated density of mCherry+ fibres from Vglut1+ (N = 3, 3-4 sections/mouse) and Vglut2+ (N = 3, 3-4 sections/mouse) neurons (unpaired Student's t-test for total CeA, Vglut1 vs Vglut2, t = 9.98, df = 25, p < 0.0001. Two-way ANOVA, CeM vs CeL, strain X region, $F_{(1,50)}$ = 14.0, p < 0.001; Bonferroni's post-hoc test, ****p < 0.0001. CeL includes lateral and capsular subregions. Data represented as means ± s.e.m.

K, Dual-target retrograde tracing strategy from CeA and dorsomedial hypothalamus (DMH).

L, Representative targeting of CeA.

M, Representative targeting of DMH.

N, Deposition of green and red beads in the mPFC. *Inset,* distribution of CeA and DMH projectors in different layers of DP. Red, green, and yellow arrowheads indicate red beads, green beads, and overlay, respectively.

O, Number of DP neurons projecting to CeA, DMH, or both (One-way ANOVA, $F_{(2,24)}$ = 11.1, p = 0.0004; Bonferroni's post-hoc test, **p < 0.01; N = 3, 3 sections/mouse). Data represented as means ± s.e.m.

P, Strategy for neuronal activation analysis. Seven days after injection, animals were split into three groups: home cage control, shock only, and serial compound stimulus fear conditioning (SCS-FC).

102 **Q**, Representative images showing bead+ and/or cFos+ cells in the DP. *Left*, 10x and *right*, 20x
103 magnifications. Red arrow, bead+; yellow arrow, bead and cFos+.
104 **R**, Quantification of cFos expression in bead+ cells (N = 3-4 mice; 3-4 sections/mouse; One-
105 way ANOVA, $F_{(2,34)} = 20.4$, $p < 0.0001$; Bonferroni's post-hoc test, ***$p < 0.001$, ****$p < 0.0001$).
106 Data represented as means ± s.e.m.
107
108 The DP also projects to the dorsomedial hypothalamus (DMH), and this pathway regulates
109 sympathetic responses to psychosocial stress.[18] To determine whether the DP-to-CeA and DP-
110 to-DMH pathways are discrete, we injected red or green-fluorescent retro-beads into the CeA and
111 DMH (**Fig. 1K-M**). Both red and green retro-beads were localized in DP cells (**Fig. 1N**), but the
112 DMH-projecting DP neurons were localized in layers V and VI, while CeA-projecting cells were
113 found in layers II/III (**Fig. 1N**, *inset*). Only a small number of DP cells (~8%) were co-labelled,
114 suggesting that the DP-to-CeA and DP-to-DMH pathways are largely anatomically distinct (**Fig.
115 1O**).
116
117 Given the role of the CeA in defensive response selection and the role of the DP in stress
118 responding,[2,18] we hypothesized that threats would activate CeA-projecting DP neurons. To test
119 this, we injected C57BL/6J mice with retro-beads in the CeA and divided animals into three
120 groups: home cage control, shock-only, and fear conditioning (**Fig. 1P; Fig. S1B**). The fear
121 conditioning (FC) group was subjected to a protocol we developed that elicits freezing and flight
122 responses to separate components of a serial compound stimulus (SCS-FC, see **Fig. S1D** for
123 behaviour).[2] Compared to home cage control and shock-only groups, SCS-FC mice displayed
124 greater numbers of retro-bead+ cells in the DP that were co-labelled with cFos (**Fig. 1P-R**). There
125 were no significant differences in the total number of retro-bead+ cells across the groups,
126 indicating a consistent retrograde labelling efficiency across the three experimental groups (**Fig.
127 S1C**).

128

129 **DP-to-CeA neurons are activated by flight**

130 The significantly elevated expression of cFos in the SCS-FC group compared to the shock-only
131 group suggests that DP-to-CeA neurons are recruited under conditions with increased threat
132 imminence. Therefore, we set out to determine the activation patterns of DP-to-CeA projecting
133 neurons during our SCS-FC protocol, which induces escalating intensities of defensive
134 behaviours. We used an intersectional approach to selectively express GCaMP6f in DP-to-CeA
135 projection neurons and imaged their *in-vivo* calcium activity in unrestricted mice using custom-
136 built open-source miniscopes (**Fig. 2A-C; Fig. S2A-D**). We observed comparable levels of
137 activation to the tone and white noise (WN) components of the SCS task during preconditioning.
138 Moreover, there was no correlation between calcium activity and movement speed before
139 conditioning (**Fig. S2E-G**). Following conditioning, mice exhibited elevated levels of freezing to
140 the tone and flight to the WN in the conditioning context (hereafter called the high-threat context),
141 consistent with our previous findings (**Fig. 2D; Fig. S2A-D**).[2,21] By contrast, mice exhibited only
142 freezing when exposed to the same conditioned stimuli in a neutral context (hereafter called the
143 low-threat context; **Fig. 2E; Fig. S2D,H**). Although there was variability in flight scores seen in
144 mice fitted with miniscopes, this was related to the miniscope rather than the implantation surgery,
145 as non-implanted but miniscope-fitted control mice showed a similar pattern of flight scores (**Fig.
146 S2I-J**).

147

148 The CeA-projecting DP neuronal population was most active during WN and shock in the high-
149 threat context (**Fig. 2F**). Interestingly, WN-induced activation was absent in the low-threat context
150 (**Fig. 2G**). Moreover, the mean activity of CeA-projecting DP neurons (Zscore) increased
151 concurrently with speed in the high- but not low-threat context (**Fig. 2F,G**). Many individual DP-
152 to-CeA neurons were active (neurons with peaks ≥3 s.d. above baseline) specifically during the
153 WN and post-shock periods, epochs of elevated flight behaviour (**Fig. 2H**, *left*). Activity was

154 significantly higher during WN and post-shock compared to the tone (**Fig. 2K**), further suggesting
155 that DP-to-CeA neuronal activity is more associated with higher-intensity threats. Transient
156 calcium events to both cues were observed in the low-threat context (**Fig. 2H**, *right*), yet no
157 significant difference was observed for Z-scores between tone and WN (**Fig. 2L**), paralleling the
158 lack of flight behaviour (**Fig. 2E,G**).
159
160 Among individual responsive cells, most neurons responded during the WN and post-shock
161 period in the high-threat context, while neuronal responses were more evenly distributed across
162 response categories in the low-threat context (**Fig. 2I**). In the high-threat context (day 3), a higher
163 percentage of cells encoded stimuli that produced flight (WN and shock; 41%) as compared to
164 cells that encoded stimuli producing freezing (tone; 4.6%; **Fig. 2J**). In the low-threat context (day
165 4), where flight was not observed, the proportions of neurons that responded to the tone or WN
166 (16% and 16.6%) were comparable. Concomitant with a reduction in threat intensity, the
167 percentage of WN-responsive neurons decreased from 27.3% in the high-threat context to 12.3%
168 in the low-threat context (**Fig. 2J**). Together, these data demonstrate that the DP-to-CeA
169 population encodes high-intensity threats in a context-specific manner.
170
171 We next assessed if the activity of the threat-encoding cells correlated with behavioural state. We
172 analysed data from the last three trials in the high-threat context, when flight scores during the
173 WN were maximal (**Fig. 2D**). We found that the activity of threat-responsive neurons positively
174 correlated with speed and negatively correlated with freezing (**Fig. 2M**). In the low-threat context,
175 the positive correlation between Zscore and speed was greatly reduced, and there was no
176 significant correlation with freezing (**Fig. 2N)**, further suggesting that the DP-to-CeA pathway is
177 linked to flight behaviour under high-threat conditions.

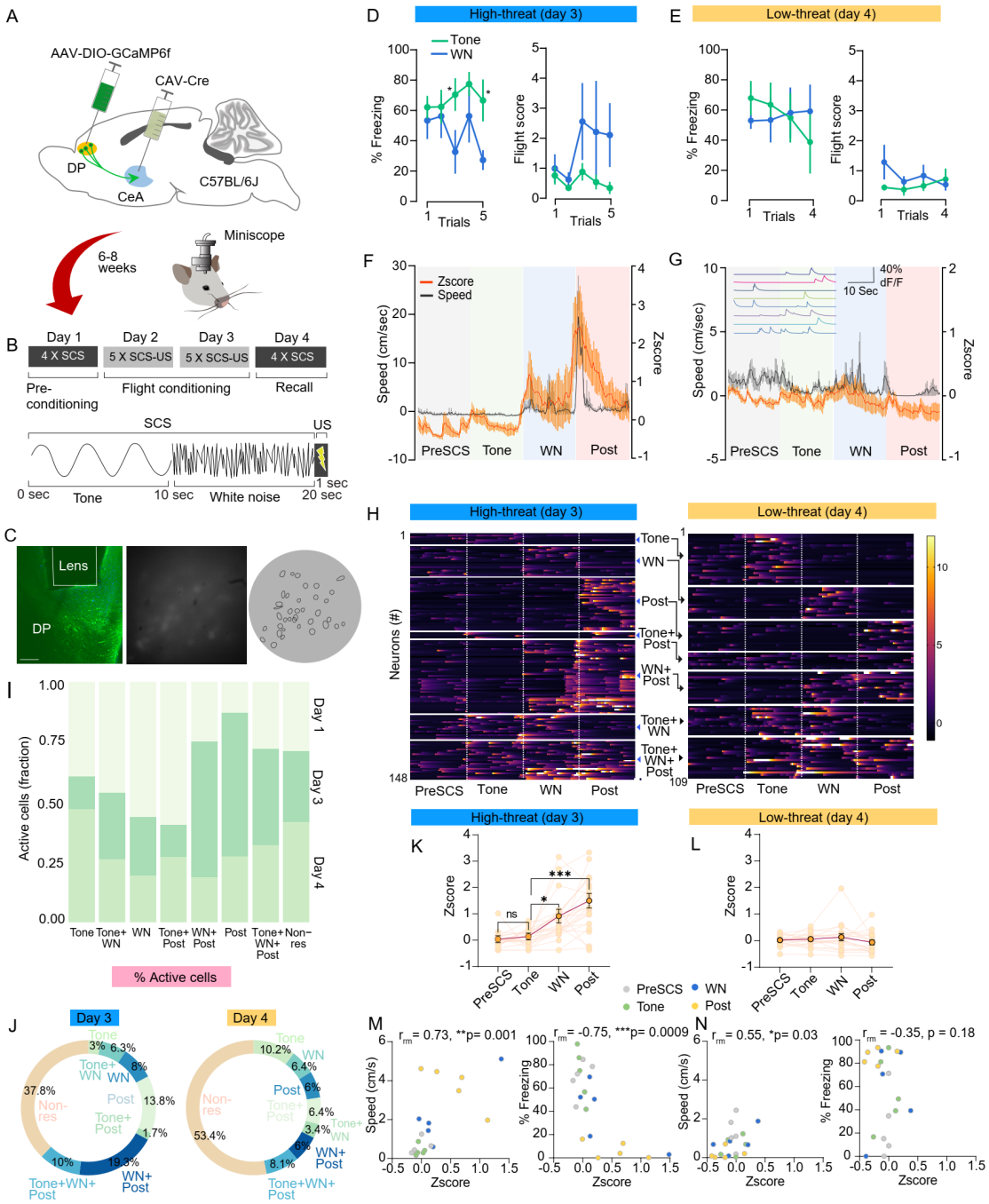

Figure 2: DP-to-CeA projecting cells are activated by high fear states.

A, Schematic of the intersectional strategy used to record DP-to-CeA projector activity.

B, Implanted mice were subjected to a fear conditioning paradigm designed to elicit high fear states.

183 **C**, *Left*, Representative GCaMP6f expression with lens placement in the DP (scale bar = 500
184 μm). *Right*, miniscope field-of-view (raw and post cell extraction).
185 **D**, Freezing and flight scores in the high-threat context. N = 5
186 **E**, Freezing and flight scores in the low-threat context. N = 5
187 **F**, Zscores of active neurons and speed in the high-threat context (N = 148 neurons).
188 **G**, Zscores of active neurons and speed in the low-threat context (N = 109 neurons). *Inset*,
189 representative Ca^{2+} traces (dF/F) extracted from a representative mouse.
190 **H**, Heatmap of Z-scores from active neurons during the last trial in the high-threat context (148
191 neurons from 5 mice, *left*), and from the last trial in the low-threat context, organized by
192 response profile (109 neurons from 5 mice, *right*).
193 **I**, Fraction of active cells and non-responsive cells during different sessions, categorized by
194 activity profile.
195 **J**, Percentages of neurons activated (neurons with peaks ≥3 s.d. above baseline) during
196 different cue periods in the high- (*left*) and low- (*right*) threat contexts.
197 **K**, Z-score of preSCS, tone and WN and post-shock (post) of the entire DP-to-CeA population in
198 the high-threat context (from all trials, Ordinary one-way ANOVA, effect of stimuli $F_{(3,16)} = 19.4$, p
199 < 0.0001, followed by Bonferroni's post-hoc test, *P < 0.05, ***P < 0.001). Data shown as
200 means ± s.e.m.
201 **L**, Z-score of preSCS, tone and WN and post-SCS (post) of the entire DP-to-CeA population in
202 the low-threat context (from all trials, Ordinary one-way ANOVA, effect of stimuli $F_{(3,16)} = 0.815$,
203 p = 0.504, followed by Bonferroni's post-hoc test, n.s.). Data shown as means ± s.e.m.
204 **M**, Repeated measure correlation of Z-score of active neuronal populations (N = 5 mice) with
205 speed or freezing in the high-threat context (r_{rm} = repeated measures correlation coefficient).
206 **N**, Repeated measure correlation of Z-score of active neuronal populations (N = 5 mice) with
207 speed or freezing in the low-threat context (r_{rm} = repeated measures correlation coefficient).
208

209 **DP-to-CeA neurons mediate avoidance**

210 The high prevalence of DP-to-CeA neurons active in the high-threat context suggests a functional
211 role for this pathway in negative-valence related behaviours. We first tested this idea using
212 chemogenetic manipulations of DP-to-CeA neurons in standard avoidance paradigms used to
213 assay anxiety-like states: the open field test (OFT) and the elevated plus maze (EPM). We used
214 the same intersectional targeting strategy to express either inhibitory (hM4Di-mCherry) or
215 excitatory (hM3Dq-mCherry) DREADDs in the DP-to-CeA pathway, with an mCherry only group
216 serving as a CNO control (**Fig. 3A-C**). DREADD-mediated inhibition of the DP-to-CeA pathway
217 increased the time spent by animals in the centre zone of the OFT (**Fig. 3D,F**) and in the open
218 arm of the EPM (**Fig. 3E,H**) without affecting the total distance travelled (**Fig. 3G**). By contrast,
219 chemogenetic stimulation of this pathway did not induce avoidance behaviour in either assay.
220 These findings suggest that the DP-to-CeA pathway is necessary but not sufficient for anxiety-
221 like behaviour.

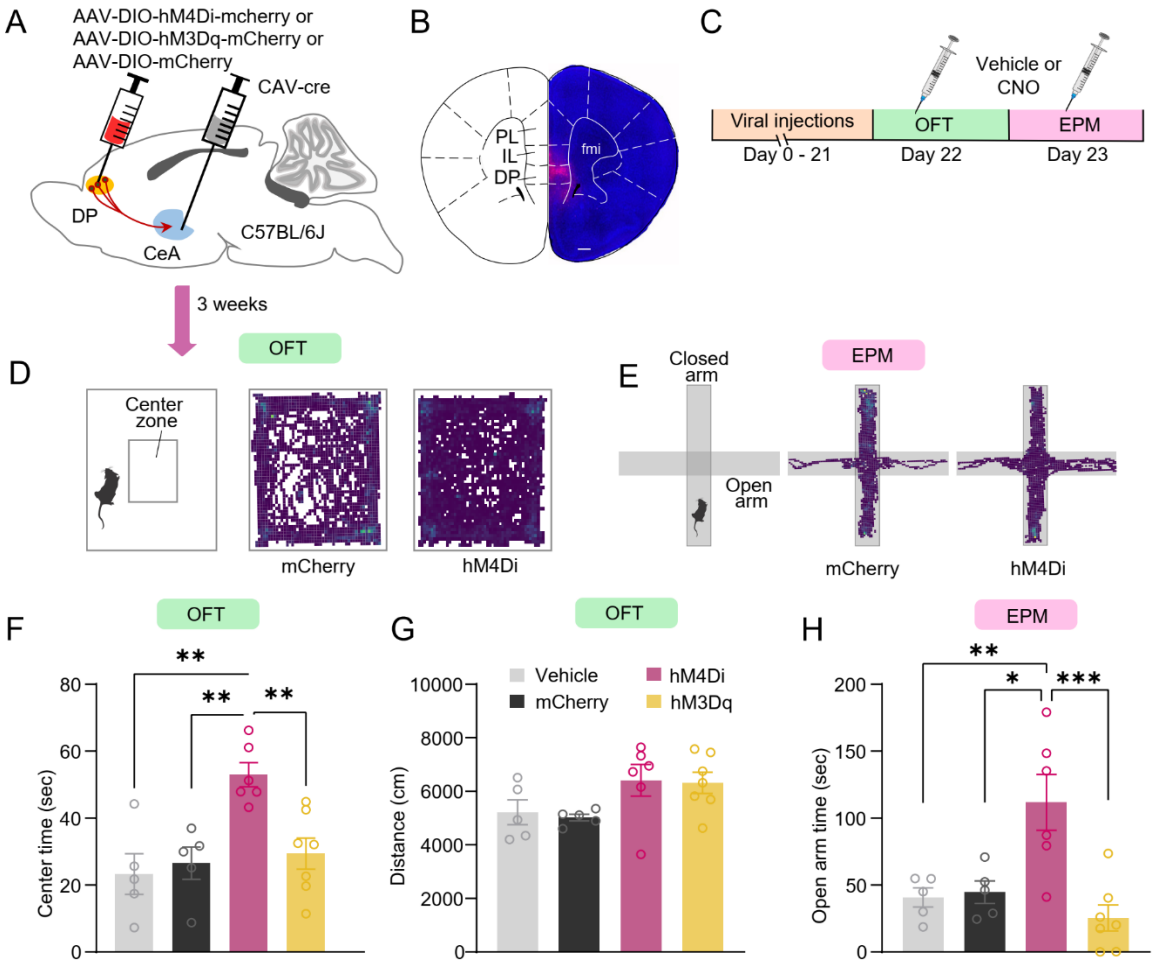

Figure 3: Chemogenetic inhibition of DP-to-CeA pathway reduces avoidance.

A, Intersectional strategy used for chemogenetic manipulation of the DP-to-CeA pathway.

B, Representative mCherry expression in the DP (scalebar = 500 μm).

C, Mice from control (hM4Di-mCherry + vehicle, N = 5; mCherry + CNO, N = 5) and DREADD (hM4Di-mCherry, N = 6; hM3Dq-mCherry, N = 7) groups were subjected to the OFT and EPM 30 min after CNO (5 mg/kg) or vehicle injection.

D, Representative activity plots of mCherry + CNO and hM4Di + CNO mice in the OFT.

E, Representative activity plots of mCherry + CNO and hM4Di + CNO mice in the EPM.

231 **F**, Inhibition of DP-to-CeA pathway significantly increased the time spent in the centre zone
232 (One-way ANOVA, $F_{(3,19)} = 8.02$, $p = 0.001$). Bonferroni's post-hoc test. $^{**}p < 0.01$. All values
233 represented as mean ± s.e.m.
234 **G**, DREADD manipulations did not alter distance travelled in the OFT (One-way ANOVA, $F_{(3,19)}$
235 $= 2.59$, $p = 0.083$).
236 **H**, inhibition of the DP-to-CeA pathway significantly increased open-arm time in the EPM (One-
237 way ANOVA, $F_{(3,19)} = 8.81$, $p = 0.0007$). Bonferroni's post-hoc test. $^{*}p < 0.05$; $^{**}p < 0.01$; $^{***}p <$
238 0.001. All values represented as mean ± s.e.m.
239
240 **DP-to-CeA neurons mediate flight**
241 To study the functional role of the DP-to-CeA pathway in fear-related behaviour, we performed
242 gain- and loss-of-function studies using optogenetics in the OFT and SCS-FC (**Fig. 4 A-B**). We
243 injected a Cre-dependent vector carrying eNpHR, ChR2, or an EYFP control into the DP and a
244 retrograde CAV2-Cre vector into the CeA of C57BL/6J mice (**Fig. 4A**). Inhibition of DP-to-CeA
245 terminals significantly increased the time spent in and number of entries into the inner zone of the
246 OFT, but did not affect locomotor activity, consistent with chemogenetic manipulations (**Fig. 4C-**
247 **E**). We used a within-subjects experimental design in the SCS-FC paradigm, with optogenetic
248 stimulation during half of the trials. In the high-threat context, inhibition of DP-to-CeA terminals
249 significantly reduced flight in response to the WN (**Fig. 4J; Fig. S3C,D**). Interestingly, inhibiting
250 these terminals also significantly elevated freezing during the WN period, consistent with the
251 concept of fear scalability (**Fig. 4I; Fig. S3A,B**).[22,23] Optogenetic inhibition had no effect on
252 defensive behaviour in the low-threat context, further supporting the role of the DP-to-CeA
253 pathway in situations of high-threat intensity (**Fig. 4K**). Optogenetic activation of DP-to-CeA
254 terminals did not elicit significant behavioural changes in the OFT, in a real-time place aversion
255 test, or in the SCS-FC paradigm (**Fig. 4F-H,L-N; Fig. S3E-H; Fig. S4A-F**). Together, these data

support an essential role of the DP-to-CeA pathway for generating flight responses exclusively in high-threat contexts.

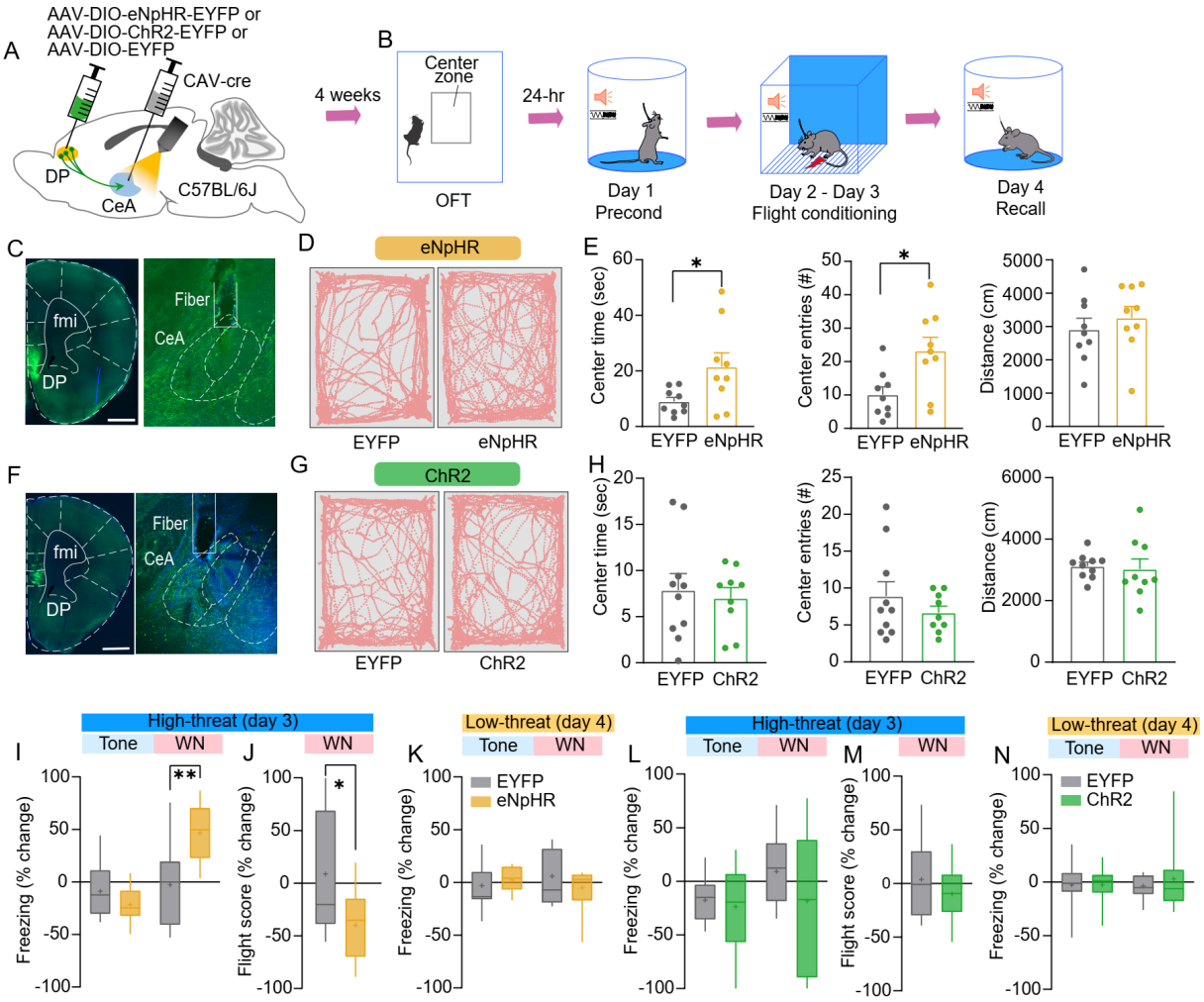

Figure 4. Optogenetic modulation of the DP-to-CeA pathway regulates flight.

A, Schematic of intersectional targeting strategy for optogenetic manipulations of DP-to-CeA pathway.

B, Experimental timeline for optogenetic inhibition and stimulation experiments.

C, Representative images of eNpHR-EYFP expression in DP and fibre stub placement in CeA (scalebar = 500 μm).

D, Representative tracking data of EYFP and eNpHR mice in the OFT.

266 **E**, Effect of optogenetic inhibition in OFT in EYFP (N = 9) and eNpHR (N = 9) groups. Unpaired
267 Student's t-test, *$p < 0.05$.
268 **F**, Representative images of ChR2-EYFP expression in DP and fibre stub placement in CeA
269 (scalebar = 500 μm).
270 **G**, Representative tracking data of mice after optogenetic stimulation in OFT.
271 **H**, Effect of optogenetic stimulation in OFT in EYFP (N = 10) and ChR2 (N = 9) groups
272 (Unpaired Student's t-test, n.s.).
273 **I**, Effect of optogenetic inhibition in EYFP (N = 9) and eNpHR (N = 9) groups on % change
274 (LED-on vs LED-off, tone and WN) in freezing in the high-threat context (EYFP vs eNpHR,
275 Mann-Whitney, ** $p < 0.01$).
276 **J**, Effect of optogenetic inhibition in EYFP (N = 9) and eNpHR (N = 9) groups on % change
277 (LED-on vs LED-off, WN) in flight scores in the high-threat context (EYFP vs eNpHR, Mann-
278 Whitney, * $p < 0.05$).
279 **K**, Effect of optogenetic inhibition in EYFP (N = 9) and eNpHR (N = 9) groups on % change
280 (LED-on vs LED-off, tone and WN) in freezing in the low-threat context (EYFP vs eNpHR,
281 Mann-Whitney, n.s.)
282 **L**, Effect of optogenetic stimulation in EYFP (N = 10) and ChR2 (N = 9) groups on % change
283 (LED-on vs LED-off, tone and WN) in freezing in the high-threat context (EYFP vs ChR2, Mann-
284 Whitney, n.s.).
285 **M**, Effect of optogenetic stimulation in EYFP (N = 10) and ChR2 (N = 9) groups on % change
286 (LED-on vs LED-off, WN) in flight scores in the high-threat context (EYFP vs ChR2, Mann-
287 Whitney, n.s.).
288 **N**, Effect of optogenetic excitation in EYFP (N = 10) and ChR2 (N = 9) groups on % change
289 (LED-on vs LED-off, tone and WN) in freezing in the low-threat context (EYFP vs ChR2, Mann-
290 Whitney, n.s.).

291 Box and whisker plots indicate median, interquartile range, and min. to max. of the distribution,
292 crosses indicate means.

293 **DP neurons control CeM outputs**

294 To investigate the mechanism by which DP neurons impact flight behaviour, we first asked
295 whether DP-to-CeA projections differentially innervate molecularly defined cell types in the CeM.
296 We targeted neurons expressing somatostatin (SOM) and corticotropin-releasing hormone (CRH)
297 because mutual inhibitory interactions between these neuronal classes mediate defensive action
298 selection in the CeL.[2] We injected AAV-syn-ChR2-mCherry into the DP and AAV-DIO-EYFP into
299 the CeA of either SOM or CRH Cre-driver lines to label SOM+ or CRH+ neurons (**Fig. 5A**).
300 Consistent with the Vglut-1 and -2 tracing experiments (**Fig. 1E-J**), only sparse DP terminals were
301 present in the CeL; however, there were many labeled terminals near both SOM+ and CRH+
302 somata in the CeM (**Fig. 5B**). We next employed slice electrophysiology and optogenetics to
303 evaluate whether SOM+ and CRH+ cells in the CeA are functionally modulated by DP projections
304 (**Fig. 5C**). DP fibre stimulation resulted in a strong induction of either a monophasic inward
305 synaptic current or a biphasic inward/outward synaptic current in both SOM+ and CRH+ neurons
306 in the CeM (**Fig. 5D,F**), but not in the CeL (**Fig. 5E,H**). The excitatory and inhibitory light-evoked
307 responses were both blocked by bath application of the AMPA receptor antagonist DNQX (**Fig.
308 5G**), indicative of a monosynaptic excitatory input as well as a disynaptic excitatory-inhibitory
309 circuit. Disynaptic responses were observed in 85% of recorded SOM+ neurons and 70% of
310 CRH+ neurons, and the amplitude of the disynaptic inhibitory response did not differ between
311 CRH+ and SOM+ neurons (**Fig. S5A**). These findings confirm the presence of functional
312 glutamatergic DP projections to the CeM but also suggest that this pathway controls flight
313 behaviour via a mechanism distinct from that which was previously described in the CeL.

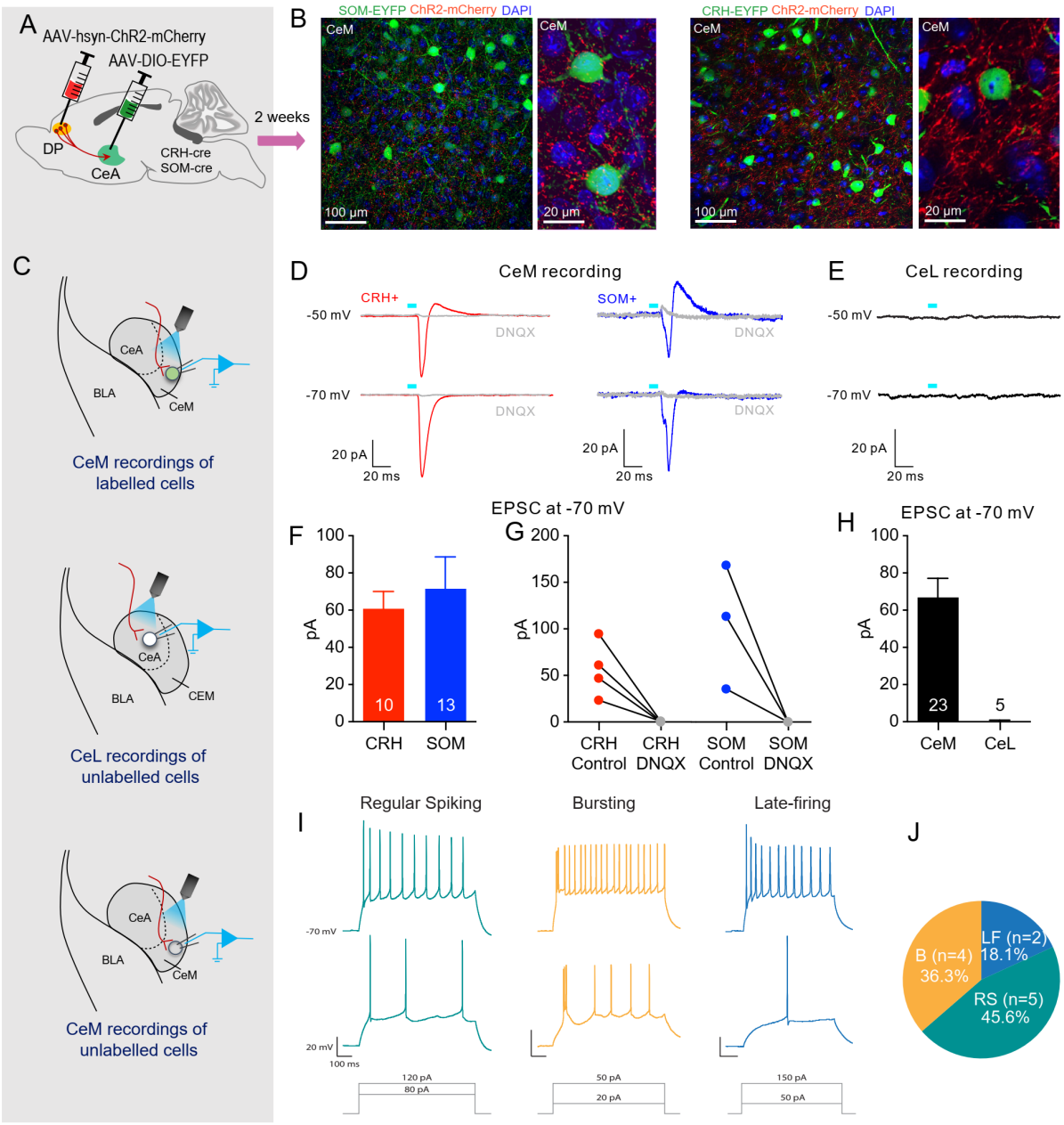

Figure 5. DP-to-CeA neurons exert excitatory control over CeM output neurons linked to flight.

A, Schematic of targeting strategy for optogenetic stimulation.

B, DP terminals in CeM near SOM+ (*left*) and CRH+ (*right*) cells at 20x and 40x magnification.

C, Schematics for recording light-evoked synaptic input from DP to CeM of SOM+ or CRH+ neurons (*top*) or unlabelled CeL (*middle*) and CeM (*bottom*) neurons.

321 **D**, Representative evoked synaptic responses in CeM SOM+ and CRH+ cells by
322 photostimulation of DP axonal fibres in voltage-clamp.
323 **E**, Photostimulation of axonal fibres did not evoke responses in CeL neurons.
324 **F**, Average amplitude of evoked EPSCs in CRH+ neurons (N = 10 cells from 3 mice) and SOM+
325 (N = 13 cells from 3 mice) at -70mV. Unpaired Student's t-test, $p = 0.63$.
326 **G**, Amplitudes of evoked EPSCs in CRH+ (N = 4 cells from 3 mice) and SOM+ (N = 3 cells from
327 2 mice) neurons at -70 mV, before and after application of DNQX.
328 **H**, Average amplitude of evoked EPSCs in CeM (N = 23 cells from 6 mice) and CeL neurons (N
329 = 5 cells from 2 mice).
330 **I**, Representative firing responses elicited in DP-excited CeM neurons.
331 **J**, Proportion of DP-excited CeM neurons classified by firing patterns (N = 11 cells from 4 mice).
332
333 CeM output neurons can be classified by their action potential firing properties[24–26], with distinct
334 categories influencing behavioural threat responding via their projections to known projection
335 targets within the periaqueductal gray (PAG).[26–28] In particular, burst firing and regular firing
336 neurons innervate columns of the PAG involved in flight responses.[26,29,30] As we did not observe
337 preferential connectivity of DP neurons to molecularly defined CeM cell types, we next asked if
338 DP innervation targeted physiologically defined CeM neuronal populations. To test which CeM
339 neurons are controlled by the DP, we classified DP-excited CeM neurons as regular spiking,
340 bursting, or late-firing. Optogenetic stimulation of DP terminals in the CeA primarily evoked
341 EPSCs in burst firing and regular firing neurons, while late-firing neurons were only rarely excited
342 (**Fig. 5I-J; Fig. S5B**). These data support a role for a DP-CeA-PAG circuit in control of flight
343 behaviour.
344
345
346

347 **Discussion**

348 Here, we define the function of a novel top-down pathway from the DP region of the mPFC directly
349 to the CeA in the control of panic-like behaviour. This non-canonical corticolimbic pathway is
350 distinct from the heavily studied reciprocal pathway between the prelimbic and infralimbic cortices
351 and the basolateral amygdala and is specifically activated in high-threat situations. Glutamatergic
352 DP neurons exert their influence via projections to the CeM, the amygdalar output nucleus known
353 for coordinating complex responses to threats. These findings have important implications for
354 understanding the basic neurobiology of threat processing.

355

356 Our study adds to a growing body of literature defining the CeA as a vital limbic brain structure
357 that integrates complex sensory information to generate survival behaviour.[23,31–33] It is
358 hypothesized that CeM output neurons control freezing through projections to the PAG,[28,34] and
359 our results demonstrate for the first time that the CeM is also important for flight. DP-to-CeA
360 projections target specific classes of CeM neurons that project to flight centres in the PAG, with
361 little innervation of neuronal classes linked to freezing.[26] It has been demonstrated that CeL circuit
362 activity is regulated by local recurrent inhibitory interactions,[2,35,36] and this mutual inhibition motif
363 is likely important for rapid action selection. Future studies should investigate whether a similar
364 "winner-take-all" motif is used in the CeM to select between freezing versus flight responses.

365

366 Learned fear behaviour is traditionally assayed using freezing, which involves the well-established
367 mPFC-basolateral amygdala-CeA pathway.[37] Previous research has shown that IL projections to
368 the basolateral amygdala and intercalated cell masses effectively operate to inhibit fear by
369 supporting fear extinction.[38,39] In contrast, the DP-to-CeA pathway defined here operates only
370 under high-threat conditions and is necessary for generating panic-like flight. Our findings
371 therefore implicate the importance of the mPFC in executive control over high-intensity fear

372 responses and may lead to a better understanding of the cortical dysfunction observed in PTSD
373 and panic disorder.[14]
374
375 **References**

376 1. Fonzo, G. A. *et al*. PTSD psychotherapy outcome predicted by brain activation during
377 emotional reactivity and regulation. *Am. J. Psychiatry* **174**, 1163–1174 (2017).
378 2. Fadok, J. P. *et al*. A competitive inhibitory circuit for selection of active and passive fear
379 responses. *Nature* **542**, 96–99 (2017).
380 3. Roelofs, K. Freeze for action: Neurobiological mechanisms in animal and human freezing.
381 *Philos. Trans. R. Soc. Lond., B, Biol. Sci.* **372** (2017).
382 4. Fanselow, M. S., Hoffman, A. N. & Zhuravka, I. Timing and the transition between modes in
383 the defensive behavior system. *Behav. Processes.* **166**, 103890 (2019).
384 5. Blanchard, D. C. & Blanchard, R. J. Defensive behaviors, fear, and anxiety. In Handbook of
385 anxiety and fear. 63–79 (Elsevier Academic Press, 2008). doi:10.1016/S1569-
386 7339(07)00005-7.
387 6. Perusini, J. N. & Fanselow, M. S. Neurobehavioral perspectives on the distinction between
388 fear and anxiety. *Learn. Mem.* **22**, 417-425 (2015).
389 7. Johnson, P. L., Truitt, W. A., Fitz, S. D., Lowry, C. A. & Shekhar, A. Neural pathways
390 underlying lactate-induced panic. *Neuropsychopharmacology* **33**, 2093-2107 (2008).
391 8. Münsterkötter, A. L. *et al*. Spider or no spider? Neural correlates of sustained and phasic
392 fear in spider phobia. *Depress. Anxiety.* **32**, 656–663 (2015).
393 9. Mobbs, D. *et al*. From threat to fear: The neural organization of defensive fear systems in
394 humans. *J. Neurosci.* **29**, 12236–12243 (2009).
395 10. Tromp, D. P. M. *et al*. Reduced structural connectivity of a major frontolimbic pathway in
396 generalized anxiety disorder. *Arch. Gen. Psychiatry.* **69**, 925–934 (2012).
397 11. Marek, R., Strobel, C., Bredy, T. W. & Sah, P. The amygdala and medial prefrontal cortex:
398 Partners in the fear circuit. *J. Physiol.* **591**, 2381-2391 (2013).
399 12. Senn, V. *et al.* Long-range connectivity defines behavioral specificity of amygdala neurons.
400 *Neuron* **81**, 428–437 (2014).
401 13. Karalis, N. *et al.* 4-Hz oscillations synchronize prefrontal-amygdala circuits during fear
402 behavior. *Nature Neuroscience* **19**, 605–612 (2016).

403 14. Andrewes, D. G. & Jenkins, L. M. The role of the amygdala and the ventromedial prefrontal
404 cortex in emotional regulation: Implications for post-traumatic stress disorder.
405 *Neuropsychol. Rev.* **29**, 220-243 (2019).
406 15. De Franceschi, G., Vivattanasarn, T., Saleem, A. B. & Solomon, S. G. Vision guides
407 selection of freeze or flight defense strategies in mice. *Curr. Biol.* **26**, 2150–2154 (2016).
408 16. Wang, W. *et al*. Coordination of escape and spatial navigation circuits orchestrates
409 versatile flight from threats. *Neuron* **109**, 1–13 (2021).
410 17. McDonald, A. J. Cortical pathways to the mammalian amygdala. *Prog. Neurobiol.* **55**, 257-
411 332 (1998).
412 18. Kataoka, N., Shima, Y., Nakajima, K. & Nakamura, K. A central master driver of
413 psychosocial stress responses in the rat. *Science* **367**, 1105–1112 (2020).
414 19. Anastasiades, P. G. & Carter, A. G. Circuit organization of the rodent medial prefrontal
415 cortex. *Trends Neurosci.* **44**, 550–563 (2021).
416 20. Fremeau, R. T. *et al*. The expression of vesicular glutamate transporters defines two
417 classes of excitatory synapse. *Neuron* **31**, 247–260 (2001).
418 21. Borkar, C. D. & Fadok, J. P. A novel pavlovian fear conditioning paradigm to study freezing
419 and flight behavior. *J Vis Exp* 1–13 (2021). doi:10.3791/61536.
420 22. Anderson, D. J. & Adolphs, R. A framework for studying emotions across species. *Cell* **157**,
421 187–200 (2014).
422 23. Fadok, J. P., Markovic, M., Tovote, P. & Lüthi, A. New perspectives on central amygdala
423 function. *Curr. Opin. Neurobiol.* **49**, 141–147 (2018).
424 24. Dumont, É. C., Martina, M., Samson, R. D., Drolet, G. & Paré, D. Physiological properties
425 of central amygdala neurons: Species differences. *Eur. J. Neurosci.* **15**, 545–552 (2002).
426 25. Duvarci, S., Popa, D. & Paré, D. Central amygdala activity during fear conditioning. *J.*
427 *Neurosci.* **31**, 289–294 (2011).
428 26. Li, J. N. & Sheets, P. L. The central amygdala to periaqueductal gray pathway comprises
429 intrinsically distinct neurons differentially affected in a model of inflammatory pain. *J.*
430 *Physiol.* **596**, 6289–6305 (2018).
431 27. Rizvi, T. A., Ennis, M., Behbehani, M. M. & Shipley, M. T. Connections between the central
432 nucleus of the amygdala and the midbrain periaqueductal gray: Topography and
433 reciprocity. *J. Comp. Neurol.* **303**, 121–131 (1991).
434 28. Tovote, P. *et al*. Midbrain circuits for defensive behaviour. *Nature* **534**, 206–212 (2016).

29. Bandler, R. & Carrive, P. Integrated defence reaction elicited by excitatory amino acid microinjection in the midbrain periaqueductal grey region of the unrestrained cat. *Brain Res.* **439**, 95–106 (1988).
30. Behbehani, M. M. Functional characteristics of the midbrain periaqueductal gray. *Prog. Neurobiol.* **46**, 575–605 (1995).
31. Keifer, O. P., Hurt, R. C., Ressler, K. J. & Marvar, P. J. The physiology of fear: Reconceptualizing the role of the central amygdala in fear learning. *Physiology* **30**, 389–401 (2015).
32. Ressler, R. L. & Maren, S. Synaptic encoding of fear memories in the amygdala. *Curr. Opin. Neurobiol.* **54**, 54–59 (2019).
33. Kong, M. S. & Zweifel, L. S. Central amygdala circuits in valence and salience processing. *Behav. Brain Res.* **410**, 113355 (2021).
34. Viviani, D. *et al*. Oxytocin selectively gates fear responses through distinct outputs from the central amygdala. *Science* **333**, 104–107 (2011).
35. Li, H. *et al*. Experience-dependent modification of a central amygdala fear circuit. *Nat. Neurosci.* **16**, 332–339 (2013).
36. Hunt, S., Sun, Y., Kucukdereli, H., Klein, R. & Sah, P. Intrinsic circuits in the CeL. *eNeuro* **4**, 1–18 (2017).
37. Tovote, P., Fadok, J. P. & Lüthi, A. Neuronal circuits for fear and anxiety. *Nat. Rev. Neurosci.* **16**, 317–331 (2015).
38. Quirk, G. J., Likhtik, E., Pelletier, J. G. & Paré, D. Stimulation of medial prefrontal cortex decreases the responsiveness of central amygdala output neurons. *J. Neurosci.* **23**, 8800–8807 (2003).
39. Bukalo, O. *et al.* Prefrontal inputs to the amygdala instruct fear extinction memory formation. *Sci. Adv.* **1**, 1–9 (2015).

462 **Methods**

463 **Animals.** Male and female C57BL/6J (Stock No: 000664, Jackson laboratories, USA) mice aged
464 8-12 weeks were used. CRH-IRES-Cre (Stock Number: 012704), SOM-IRES-Cre (Stock No:
465 013044) and Vglut1-IRES-Cre (Slc17a7-IRES2-Cre-D, Stock No: 023527) mice were used for *in-*
466 *vitro* electrophysiology (aged 5-8 weeks), and to determine anatomical connectivity between DP
467 terminals and CeA neuronal subpopulations. For Vglut subpopulation tracing, Vglut1-IRES2-Cre
468 and Vglut2-ires-cre (Stock Number: 028863) mouse lines were used. All Cre-driver lines were
469 fully backcrossed to C57BL/6J. All mice were individually housed on a 12-hr light/dark cycle with
470 *ad libitum* food and water. Behavioural experiments were performed during the light phase.
471 Animals were habituated by cupping the mouse in hand for 5 minutes each day for 2 days, before
472 the start of the experiment. All animal procedures were performed in accordance with institutional
473 guidelines and were approved by the Tulane University Institutional Animal Care & Use
474 Committee.

475 **Viruses**

476 For Cre-dependent expression of channelrhodopsin (ChR2), we used AAV5-EF1a-DIO-
477 hChR2(H134R)-EYFP-WPRE-HGHpa (Addgene 20298, a gift from Karl Deisseroth). For Cre-
478 dependent expression of halorhodopsin (eNpHR), we used AAV5-EF1a-DIO-eNpHR3.0-EYFP
479 (Addgene 26966, a gift from Karl Deisseroth). Control mice for optogenetic experiments were
480 injected with AAV5-EF1a-DIO-EYFP (Addgene 27056, a gift from Karl Deisseroth). For Cre-
481 dependent expression of excitatory DREADDs, we used AAV5-hSyn-DIO-hM3D(Gq)-mCherry
482 (Addgene 44361, a gift from Bryan Roth). For Cre-dependent expression of inhibitory DREADDs,
483 we used AAV-hSyn-DIO-hM4D(Gi)-mCherry (Addgene 44362, a gift from Bryan Roth). For Cre-
484 dependent GCaMP6f expression, we used AAV5-CAG-Flex-GcaMP6f-WPRE-SV40 (Addgene
485 100835, a gift from Douglas Kim & GENIE Project). To express Cre in C57BL/6J mice, we used

486 retrograde transporting canine adenovirus type 2 carrying Cre-recombinase (CAV2-Cre, PVM,
487 France).[40]

488 To label CRH+ and SOM+ somata in the CeA for *in-vitro* electrophysiology experiments and
489 anatomical tracing, CRH-IRES-Cre and SOM-IRES-Cre mouse lines were injected with AAV5-
490 EF1a-DIO-EYFP (Addgene 27056, a gift from Karl Deisseroth). In the same mice, we used AAV5-
491 hSyn-hChR2(H134R)-mCherry (Addgene 26976, a gift from Karl Deisseroth) to express ChR2 in
492 the DP for *in-vitro* electrophysiology. For anterograde neuronal tracing experiments in Vglut1- or
493 Vglut2-cre mouse lines, AAV5-hSyn-DIO-mCherry (Addgene 50459, a gift from Bryan Roth) was
494 injected in the DP.

495 **Surgery**

496 *Tracers/Virus injections*

497 Mice were deeply anaesthetized using 5% isoflurane (Fluriso, VetOne, Boise, ID) in oxygen-
498 enriched air (OxyVet O2 Concentrator, Vetequip, Pleasanton, CA), followed by a subcutaneous
499 injection of 2 mg/kg meloxicam (OstiLox, VetOne, Boise, ID), and then fixed into a stereotaxic
500 frame (Model 1900, Kopf Instruments, Tujunga, CA) equipped with a robotic stereotaxic targeting
501 system (Neurostar, Germany). Anesthetized mice were maintained on 2-2.5% isoflurane, and a
502 core body temperature was maintained at 36°C using a feedback-controlled DC temperature
503 controller (ATC2000, World Precision Instruments, Sarasota, FL). Eye ointment (GenTeal, Alcon,
504 Switzerland) was applied to the mouse's eyes to prevent dryness. The head was shaved, and the
505 skin was sterilized using Betadine iodine solution (Purdue Products, Stamford, CT). 2% lidocaine
506 (0.1 ml, Lidocaine 2%, VetOne, Boise, ID) was injected subcutaneously at the site of incision and
507 a midline incision was made with a scalpel to expose the skull.

508 For the retrograde neuronal tracings, retrogradely transported beads (0.2 µl, 1:2 diluted with
509 saline, Lumafluor Inc., Durham, NC) were stereotaxically injected into the respective brain
510 regions. We injected CAV2-Cre into the CeA, and Cre-dependent AAV opsins or DREADD
511 vectors into the DP. Approximately 0.4 µl per hemisphere of each vector was delivered bilaterally
512 into the respective brain regions using pulled glass pipettes (tip diameter 10-20 µm, PC-100 puller,
513 Narishige, Japan), connected to a pressure ejector (PDES-Pressure Application System, npi
514 electronic equipment, Germany). For *in-vitro* electrophysiology, AAV-ChR2-mCherry was injected
515 into the DP and Cre-dependent AAV-DIO-EYFP was injected into the CeA of CRH-IRES-Cre or
516 SOM-IRES-Cre mice. AAV-DIO-mCherry was injected into the DP of Vglut1-/Vglut2-Ires-Cre
517 mice. For calcium imaging, C57BL/6J mice were injected unilaterally with CAV2-cre in the CeA
518 and Cre-dependent GCaMP6f in the DP.

519 The CeA coordinates used were: 1.2-1.3 mm posterior to bregma, ±2.9-3.0 mm lateral to the
520 midline and 4.1-4.3 mm below the dura. The DP coordinates used were 1.8-1.9 mm anterior to
521 bregma, ±0.4-0.5 mm lateral to the midline and 3.1-3.2 mm below the dura. The DMH coordinates
522 used were 1.7 mm posterior to bregma, ±0.5 mm lateral to the midline and 5 mm below the dura.

523 *Fibre implantation for optogenetics*

524 For optogenetic manipulations of behaviour, animals were bilaterally implanted with LC optic fibre
525 stubs (fibre: 0.48 NA, 200-230 µm diameter, 6 mm length, Plexon) two weeks after viral vector
526 injection. Optic fibre tips were lowered to 100–200 µm above the CeA. Implants were fixed to the
527 skull with two miniature screws (00.90-100-M-SS-FH, US Micro Screw, Seattle, WA),
528 cyanoacrylate glue gel (SuperGlue, The original super glue, Ontario, CA) and dental cement
529 (Ortho-Jet powder and black liquid acrylate, Lang, Wheeling, IL). Experiments were conducted 3
530 weeks after viral infections, to ensure adequate opsin expression.

531 *Lens implantation for Ca^{2+} Imaging*

532 Gradient index (GRIN) lens implantation surgery was performed as described previously.[41,42] Mice
533 were head fixed on the stereotaxic apparatus and a craniotomy was drilled over the DP
534 coordinates, using 1.2 mm diameter round drill burr (Harvard Apparatus, Holliston, MA). Three
535 additional holes were drilled to implant stainless steel screws (US Micro Screw, 00.90-100-M-SS-
536 FH). The skull surface was cleaned from bone fragments and wiped using sterilized cotton tips.
537 We aspirated the overlying tissue up to 1-1.5 mm above the site of implantation with a bent 27G
538 needle (NE-4527, Component supply, Sparta, TN) and performed intermittent sterile saline
539 washes to reduce intracranial pressure and improve the quality of the imaging site. A GRIN lens
540 (1 mm diameter, 9 mm length, 0.5 NA, 1 pitch, part # 1050-002177, Inscopix, Palo Alto, CA) was
541 attached to the stereotaxic arm using a custom-built lens holder, and lowered for 3 mm over the
542 course of 10 min. When the lens reached the required depth, Kwik-Sil (World Precision
543 Instruments, Sarasota, FL) was used to fill in the gap between the lens and the skull and left to
544 dry for 5 min. To hold the lens firmly in place, an adhesive cement (C&B S399 Metabond Quick
545 Adhesive Cement System Parkell, Edgewood, NY) mixed with liquid polymer (Catalyst + Quick
546 Base) was applied around the lens. After that, dental acrylic cement (Ortho-Jet powder and clear
547 liquid acrylate) was applied over the skull and screws and allowed to dry completely. The lens
548 holder was loosened and carefully detached from the lens. The layers of dental cement mixed
549 with black acrylate (Ortho-Jet powder and black liquid acrylate) were applied around the lens until
550 the height was ~0.5 mm below the top of the lens, and a thick layer of Kwik-cast (World Precision
551 Instruments, Sarasota, FL) was applied over the lens until it was embedded. This ridge around
552 the lens prevented lens damage during homecage activity and was used later for baseplate
553 implantation. Animals were then returned to the homecage, individually housed, and allowed to
554 recover for 2-3 weeks.

555 *Baseplating and verification of Ca^{2+} transients*

556 Mice were checked weekly for GCaMP6f fluorescence and Ca^{2+} transient activity over several
557 weeks after the lens implantation, as described before.[42] For baseplating, mice were anesthetized
558 with 5% isoflurane, fitted into the stereotaxic frame, and then maintained at 1%. A head-mounted
559 miniscope (UCLA open-source, http://miniscope.org/) was fixed on a custom-built holder that was
560 attached to the stereotaxic arm.[43] The focusing mechanism of the miniscope was set at mid-range
561 to leave enough distance for focus adjustments in either direction. The coaxial cable from the
562 miniscope was attached to the data acquisition box (DAQ-V3.2, UCLA), which was connected to
563 the computer through USB 3.0. The baseplate was attached to the bottom of the miniscope. We
564 aligned the miniscope objective lens over the relay lens implanted in the mouse brain, and the
565 miniscope was moved to approach the relay lens. The recording software (Miniscope controller,
566 UCLA) was turned on and LED light intensity (25%), gain, and frame rate (30 fps) were set. To
567 ensure maximum field of view and focus on the centre of the lens, the miniscope tilt was adjusted
568 to view all edges of the relay lens. Then, the miniscope was slowly moved in X, Y, Z planes to
569 locate active cells/transients. If there were no transients, the mouse was returned to the
570 homecage and checked again the following week.

571 If Ca^{2+} transients were observed, they were further confirmed using tail pinch. If multiple cells
572 were observed, these mice were then considered for baseplating. After finding the optimal focal
573 plane and clear field of view, the baseplate was fixed on the mouse skull. Dental cement mixed
574 with black acrylate (Ortho-Jet powder and black liquid acrylate) was applied layer-by-layer
575 between the baseplate and the circular ridge built during lens implantation. The dental cement
576 was applied sufficiently so that no light could pass through from the outside. After the cement was
577 dry, the miniscope was detached and a plastic cover was installed to protect the relay lens.

578 A control group of C57BL/6J mice (N = 4) were injected with the GCaMP6f virus in DP and CAV-
579 Cre in CeA but were not implanted with lenses to control for the lens implantation damage-induced
580 behaviour. Mice underwent identical conditioning as described above (**Fig. S2I-J**).

581 **Miniscope recordings**

582 Animals with Ca^{2+} transients were used for behavioural experiments (N = 5). First, the mice were
583 subjected to preconditioning on day 1, and their behaviour as well as Ca^{2+} responses were
584 recorded. Animals were conditioned in the high-threat context for 2 days (5 trials/day), followed
585 by recall in the low-threat context on day 4 (4 trials/day). The Ca^{2+} response data was at 30
586 frames/sec rate. Behaviour was simultaneously recorded to video ("Pike" camera, Allied vision,
587 Germany). Neuronal recordings were started 10 s before the start of each trial (at the onset of
588 preSCS) and turned off 10 sec after the end of shock/ cue (post-shock/cue), while behaviour was
589 continuously recorded.

590 **Ca^{2+} imaging processing.**

591 Ca^{2+} imaging videos were concatenated using ImageJ software
592 (https://imagej.nih.gov/ij/download.html). The concatenated videos were then processed using
593 MATLAB and an open source analysis package (https://bahanonu.github.io/ciatah/) as described
594 previously.[42] The videos were pre-processed by correcting for motion and temporally
595 downsampled by a factor of six. After pre-processing the videos, we extracted individual neurons
596 and their activity traces by using the open-source package Constrained Nonnegative Matrix
597 Factorization for microEndoscopic data (CNMF-E; https://github.com/zhoupc/CNMF-E). The
598 extracted cells were then manually identified based on the spatial filter and activity trace of each
599 candidate cell along with the candidate cells' average Ca^{2+} transient waveform. Data were
600 averaged over a 200 ms sliding window. The data was normalized by calculating Zscores
601 (subtracting mean activity scores during all preSCS trials from each activity trace, divided by the
602 standard deviation of each cell during all preSCS trials) and the neurons with peaks that were ≥3
603 s.d. above baseline were considered as active neurons. To determine statistically significant

604 changes in responses of the DP-to-CeA projecting cells to the tone and WN, the Zscores from
605 the corresponding periods were averaged and compared.

606 After finishing the experiments animals were perfused and their brains were isolated to confirm
607 the lens placements. The data from animals with correct lens placement was used for analysis.

608 **Behavioural paradigms**

609 *Conditioned flight paradigm*

610 Two different contexts were used. Context A (low-threat context) consisted of a clear cylindrical
611 chamber with a smooth floor, while Context B (high-threat context) consisted of a square
612 enclosure with an electrical grid floor used to deliver alternating current footshocks (ENV-414S,
613 Med Associates Inc., Fairfax, VT). These two chambers were cleaned with 1 % acetic acid and
614 70 % ethanol, respectively. A speaker (ENV-224AM, Med Associates Inc.) was mounted above
615 the chambers to deliver auditory stimuli at 75 dB. A programmable audio generator (ANL-926,
616 Med Associates, Inc.) generated auditory stimuli. Behavioural protocols were generated using
617 MedPC software (Med Associates, Inc.) to control auditory stimuli and footshock via TTL pulses.

618 We used a four-day paradigm as described previously.[2,21] On Day 1, animals were subjected to
619 pre-exposure in context A. After a 3 min baseline period, there were 4 presentations of a serial
620 compound stimulus (SCS, 20 s long) with a 90 s average pseudorandom intertrial interval (ITI)
621 (range 80−100 s). The SCS consisted of a 10 s tone (7.5 kHz, 500 ms pips at 1 Hz) and a 10 s
622 white noise (WN, random distribution of 1 to 20,000 Hz, 500 ms pips at 1 Hz). The total duration
623 of the pre-exposure session was 590 s. On Day 2 and Day 3 (conditioning days), mice were
624 placed in Context B and, after a 3 min baseline period, presented with five pairings of the SCS
625 with a 120 s average pseudorandom ITI (range 90−150 s) co-terminating with a 1 s, 0.9 mA
626 footshock. Each conditioning session lasted for 820 s. Recall session on day 4 was conducted in

627 Context A. Following a 3 min baseline period, mice were presented with 4 trials of the SCS without
628 footshock, with a 90 s average pseudorandom ITI (range 80−100 s) over a total period of 590 s.

629 For optogenetic experiments the mice were presented with 8 trials on Day 3 with 4 pairs of
630 alternating light ON-OFF trials. During recall mice were presented with 3 pairs of alternating light
631 ON-OFF trials.

632 *Quantification of defensive behaviour*

633 All sessions were recorded to video, and behaviour was analysed using contour tracking
634 (Cineplex software, Plexon, Dallas, TX). Freezing was defined as a complete cessation of
635 movement for at least 1 s and was automatically scored using a frame-by-frame analysis of pixel
636 changes (Cineplex Editor, Plexon). Results were confirmed by a trained observer blinded to
637 condition. By determining a calibration coefficient using the chambers' known size and the
638 camera's pixel dimensions, speed (cm/s) was extracted using the animal's centre of gravity.[21]
639

640 Escape jumping was scored manually from video files by a blinded observer. Flight scores were
641 calculated by dividing the average speed during each CS by the average speed during the 10 s
642 pre-CS from all the trials (baseline, BL) and then adding 1 point for each escape jump (speedCS/
643 speedBL + # of jumps). A flight score of 1 therefore indicated no change in flight behaviour from
644 the preSCS period.
645

646 *Open field test*

647 A 45 x 45 x 45 cm arena made of white opaque Plexiglas was used. The arena was cleaned using
648 70% ethanol after each mouse. Mouse behaviour was tracked under 100 lux light conditions using
649 a top-mounted camera ("Pike" camera, Allied vision, Germany).
650 *For chemogenetic* experiments, the OFT duration was 10 min.

651 *For optogenetic experiments*, the OFT duration was 6 min. After a 120 s baseline period, 4, 30
652 sec ON-OFF trials of light stimulation were used. For eNpHR experiments, a continuous orange
653 light was used at 10 mW power at the fibre tip, and for ChR2 experiments, 10 ms pulses of blue
654 light were used at 10 Hz, and 10 mW power at the fibre tip.
655 The time spent in the inner zone, the number of entries into it, and total distance traveled were
656 measured using tracking software (Cineplex Studio, Plexon).
657
658 *Elevated plus maze*
659 Behaviour was tracked using a top-mounted camera ("Pike" camera, Allied vision, Germany) for
660 10 min. The maze was made from white opaque Plexiglas material and consisted of four 30 cm
661 long and 7 cm wide arms. Two open arms had no walls, and two enclosed arms had 15 cm high
662 walls. The maze was elevated 40 cm above the ground. The arena was cleaned using 70%
663 ethanol after every test. The total time spent in the open arms was calculated using Cineplex
664 Editor software (Plexon).
665
666 **Chemogenetic manipulations of behaviour**
667 Behavioural testing was performed 3-4 weeks after viral injections. First, mice were subjected to
668 the OFT. On the next day, animals were subjected to the EPM, and 4 hr later to preconditioning.
669 For the next 2 days, mice were flight conditioned, followed by a recall session on the final day. 30
670 min before the start of behavioural testing animals were injected with clozapine N-oxide [CNO;
671 0.5 mg/ml in vehicle (0.9% saline), given as 10 ml/kg for final dose of 5 mg/kg, intraperitoneally
672 (ip); Enzo Life Sciences, Farmingdale, NY] or vehicle (10 ml/kg volume, ip).
673
674 **Optogenetic manipulations of behaviour**
675 Two weeks after vector injection, animals were implanted with fibre stubs (Plexon) targeting CeA,
676 as described in Surgery. For optogenetic modulation, we used a Plex controller system (Plexon)

677 operated through Radiant software (Plexon). Two PlexBright LED modules (Plexon) were
678 connected to the controller, and an LC patch cable (200-230 μm fibre, 1 meter long, 0.66 NA,
679 Plexon) was connected. Laser power at the fibre tip was measured before every test with an
680 optical power and energy meter (PM100D, ThorLabs, Newton, NJ). The patch cable was
681 connected to the head-mounted fibre stubs using ceramic sleeves. Connectors were tested for
682 coupling efficiency before implantations, and laser power at the fibre tip for behavioural
683 manipulations was adjusted to reach a value of 10 mW.
684
685 Experiments were performed with a within-subjects design in which mice underwent eight trials
686 during FC2 with alternating 2 trials with lights on and 2 trials with lights off. During recall session,
687 mice underwent six trials with alternating light on off conditions. To inhibit (eNpHR) DP-CeA
688 neuronal populations during threat cues, a 620 nm light was switched on 500 ms before the onset
689 of the SCS (first tone pip) and remained on until the end of the last white noise pip (20.5 s in total).
690 For ChR2-induced excitation of DP-to-CeA neuronal populations, we used 465 nm light pulses
691 (10 Hz, 10 ms width) which was switched on 500 ms before the onset of the SCS (first tone pip)
692 and remained on until the end of the last white noise pip (20.5 s in total).

693 **Real-time place aversion test**

694 To test whether optogenetic stimulation of the DP-to-CeA pathway induced aversive responses,
695 we subjected the AAV-DIO-ChR2-EYFP or AAV-DIO-EYFP-injected mice to real-time place
696 aversion test for 10 min. We used a custom-made 50 × 50 × 50 cm arena made from white opaque
697 Plexiglas and divided into two equal compartments. One side of the chamber was allotted as the
698 stimulation side and other as a neutral side (non-stimulated, with striped walls and metallic plate
699 floor). Mice were placed in the non-stimulated side, and 10 or 20 Hz blue LED light stimulation
700 was delivered each time the mouse moved to the stimulation side of the chamber. The light
701 stimulation was continuously on until the mouse moved back into the non-stimulation

702 compartment. Behaviour was recorded via a top mounted recording camera attached to recording
703 system (Plexon) and scored using Cineplex editor (Plexon) by a blinded experimenter. The %
704 time spent in the stimulation chamber was used as a measure of aversion.
705
706 **Immunohistochemistry (IHC)**
707 Following the completion of experiments, mice were anesthetized with tribromoethanol (240
708 mg/kg) and perfused transcardially with phosphate-buffered saline (PBS) followed by 4%
709 paraformaldehyde in PBS. Brains were isolated and stored in paraformaldehyde overnight. On
710 the next day, fixed brains were sectioned using a vibrating microtome (Precisionary, Greenville,
711 NC) in 60- (for cFos IHC) or 80-µm thick coronal slices.
712
713 Antibody staining was performed on floating tissue sections. Briefly, sections were washed in
714 PBS-TritonX100 (PBST, 0.3%) and blocked using 5% goat serum in PBST for 1 hr followed by an
715 overnight (for RFP or GFP staining), or 48-h (for cFos staining), incubation in primary antibodies
716 at 4°C. Primary antibodies used in this study were rabbit anti-RFP (1:1500, 600-401-379,
717 Rockland Immunochemicals, Pottstown, PA), chicken anti-GFP (1:2000, NB100-1614, Novus
718 Biologicals, USA), rabbit anti-cFos (1:1000, 226003, Synaptic Systems, Germany). After primary
719 antibody incubation, sections were washed in PBST and incubated in secondary antibodies in
720 PBST (1:500 goat anti-rabbit AlexaFluor 555/488 or goat anti-chicken AlexaFluor 488, Thermo
721 Fisher Scientific, USA). Following final rinses with PBS, sections were mounted and scanned from
722 the DP and CeA.
723 Images were obtained using an Axio Scan.Z1 slide-scanning microscope (Zeiss, Germany) and
724 a confocal microscope (FV3000, Olympus, Japan). Mice were included in subsequent data
725 analyses only if bilateral expression specific to the target region was observed.

726 **cFos quantification**

727 Red fluorescent retro-beads were injected into the CeA of C57BL/6J mice. 7 days later, animals
728 were divided into 3 groups: homecage control, shock-only, and SCS-FC. Shock-only and SCS-
729 FC mice were subjected to two days of conditioning and were sacrificed 90 min after the second
730 session by transcardial perfusion. Following brain sectioning and IHC staining for cFos, confocal
731 images were taken. The quantification of cFos+, bead+, and cells with both markers were
732 performed by a blinded observer using ImageJ.
733
734 **Brain slice electrophysiology**
735 *Slice preparation:* Coronal brain slices containing the CeA were collected from mice at least two
736 weeks after viral injections for *ex vivo* electrophysiological recordings, as described earlier.[36,44]
737 Mice (6 to 9 weeks) were decapitated in a restraining plastic cone (DecapiCone, Braintree
738 Scientific, Braintree, MA) and the brains were dissected and immersed in ice-cold, oxygenated
739 cutting solution containing the following (in mM): 252 sucrose, 2.5 KCl, 26 $NaHCO_3$, 1 $CaCl_2$, 5
740 $MgCl_2$, 1.25 NaH_2PO_4, 10 glucose. The brains were trimmed and glued to the chuck of a Leica
741 VT-1200 vibratome (Leica Microsystems, Germany) and 300 µm-thick coronal slices were
742 sectioned. Slices were transferred to a holding chamber containing oxygenated recording artificial
743 cerebrospinal fluid (aCSF) containing (in mM): 126 NaCl, 2.5 KCl, 1.25 NaH_2PO_4, 1.3 $MgCl_2$, 2.5
744 $CaCl_2$, 26 $NaHCO_3$, and 10 glucose. They were maintained in the holding chamber at 34°C for 30
745 min before decreasing the chamber temperature to ~20°C.
746
747 *Patch clamp recording:* Slices were bisected down the midline and hemi-slices were transferred
748 from the holding chamber to a submerged recording chamber mounted on the fixed stage of an
749 Olympus BX51WI fluorescence microscope equipped with differential interference contrast (DIC)
750 illumination. The slices in the recording chamber were continuously perfused at a rate of 2 ml/min
751 with recording aCSF maintained at 32-34°C and continuously aerated with 95% O_2/5% CO_2.
752 Whole-cell patch clamp recordings were performed in eYFP-labeled SOM+ or CRH+ neurons or

753 unlabeled neurons in the CeM, and neurons in the CeL. Glass pipettes with a resistance of 4-6
754 MΩ were pulled from borosilicate glass (ID 1.2mm, OD 1.65mm) on a horizontal puller (Sutter P-
755 97) and filled with an intracellular patch solution containing (in mM): 130 potassium gluconate, 10
756 HEPES, 10 phosphocreatine Na_2, 4 Mg-ATP, 0.4 Na-GTP, 5 KCl, 0.6 EGTA; pH was adjusted to
757 7.25 with KOH and the solution had a final osmolarity of ~ 290 mOsm. DNQX (20 uM) was
758 delivered via the perfusion bath. Series resistance was normally below 15 MΩ immediately after
759 break-in and was continuously monitored. Cells were discarded when the series resistance
760 exceeded 30 MΩ. An optical fibre was placed approximately 2 mm above the slice and ChR2-
761 expressing DP fibres were stimulated by 465 nm LED illumination (single 10-ms pulses,15 mW
762 power, delivered at 1 Hz). To assess firing properties in CeA neurons that displayed fast synaptic
763 responses, 500-750 ms depolarizing current injections were applied in current clamp mode. Data
764 were acquired using a Multiclamp 700B amplifier, a Digidata 1440A analog/digital interface, and
765 pClamp 10 software (Molecular Devices, San Jose, CA). Recordings were filtered at 4 KHz and
766 sampled at 50 KHZ. Data were analyzed with Clampfit 10 (Molecular Devices, San Jose, CA).
767 Statistical comparisons were conducted with a paired or unpaired Students's *t* test ($p < 0.05$ with
768 a two- tailed analysis was considered significant).
769

770 **Statistical analysis**

771 Data were analyzed for statistical significance using Prism 9 (GraphPad Software, San Diego,
772 CA). Statistical significance was set at $p < 0.05$. Data were tested for normal distribution using the
773 Shapiro-Wilk normality test (α=0.05). For pairwise comparisons, the appropriate parametric
774 (unpaired Student's t-test) or nonparametric (Mann-Whitney test) test was performed. Data with
775 more than two study groups were analyzed using one-way ANOVA followed by Bonferroni's post-
776 hoc tests. For calcium imaging data analysis, we used custom code written in MATLAB. Repeated
777 measures correlations were performed using the rmcorr package in R.[45] The sample size was
778 determined based on previously published research.

Methods References

40. Soudais, C., Laplace-Builhe, C., Kissa, K. & Kremer, E. J. Preferential transduction of neurons by canine adenovirus vectors and their efficient retrograde transport in vivo. *FASEB J.* **15**, 2283–2285 (2001). Doi: 10.1096/fj.01-0321fje.
41. Resendez, S. L. *et al*. Visualization of cortical, subcortical and deep brain neural circuit dynamics during naturalistic mammalian behavior with head-mounted microscopes and chronically implanted lenses. *Nat. Protoc.* **11**, 566–597 (2016).
42. Corder, G. *et al*. An amygdalar neural ensemble that encodes the unpleasantness of pain. *Science* **363**, 276–281 (2019).
43. Ghosh, K. K. *et al.* Miniaturized integration of a fluorescence microscope. *Nat. Methods* **8**, 871–878 (2011).
44. Chen, C. *et al.* Astrocytes amplify neuronal dendritic volume transmission stimulated by norepinephrine. *Cell Rep.* **29**, 4349-4361.e4 (2019).
45. Bakdash, J. Z. & Marusich, L. R. Repeated measures correlation. *Front. Psychol.* **8**, 1–13 (2017).

Acknowledgements

We thank Dr. Biafra Ahanonu (University of California, San Francisco) for providing MATLAB codes and assistance with calcium imaging data analysis. We thank Dr. Ricardo Mostany (Tulane University) for help in standardization of calcium imaging. This work was supported by the Louisiana Board of Regents through the Board of Regents support fund (**LEQSF(2018-21)-RD-A-17**) and *the National Institute of Mental Health* of the National Institutes of Health under award number **R01MH122561**. The content is solely the responsibility of the authors and does not necessarily represent the official views of the National Institutes of Health.

Author contributions:

Conceptualization— CDB, JPF; Formal analysis— CDB, XF, CS, MD, QEL, RV, CV, SB, AD, EB, AR, JP, JPF; Funding acquisition— JPF; Investigation— CDB, XF, CS, QEL; Methodology— CDB, MD, JPF; Project Administration / Supervision— CDB, JPF, JT

Resources— JPF, JT; Visualization— CDB, CS, MD, XF, JPF; Writing, original draft— CDB, JPF; Writing, review & editing— CDB, MD, XF, CS, JT, JP, JPF

Competing Interest Statement

The authors declare no competing interests.

Additional Information

Correspondence and requests for materials should be addressed to JPF.

Data availability

Data sets included in this study are available from the corresponding author upon reasonable request.

821 **Extended Data**

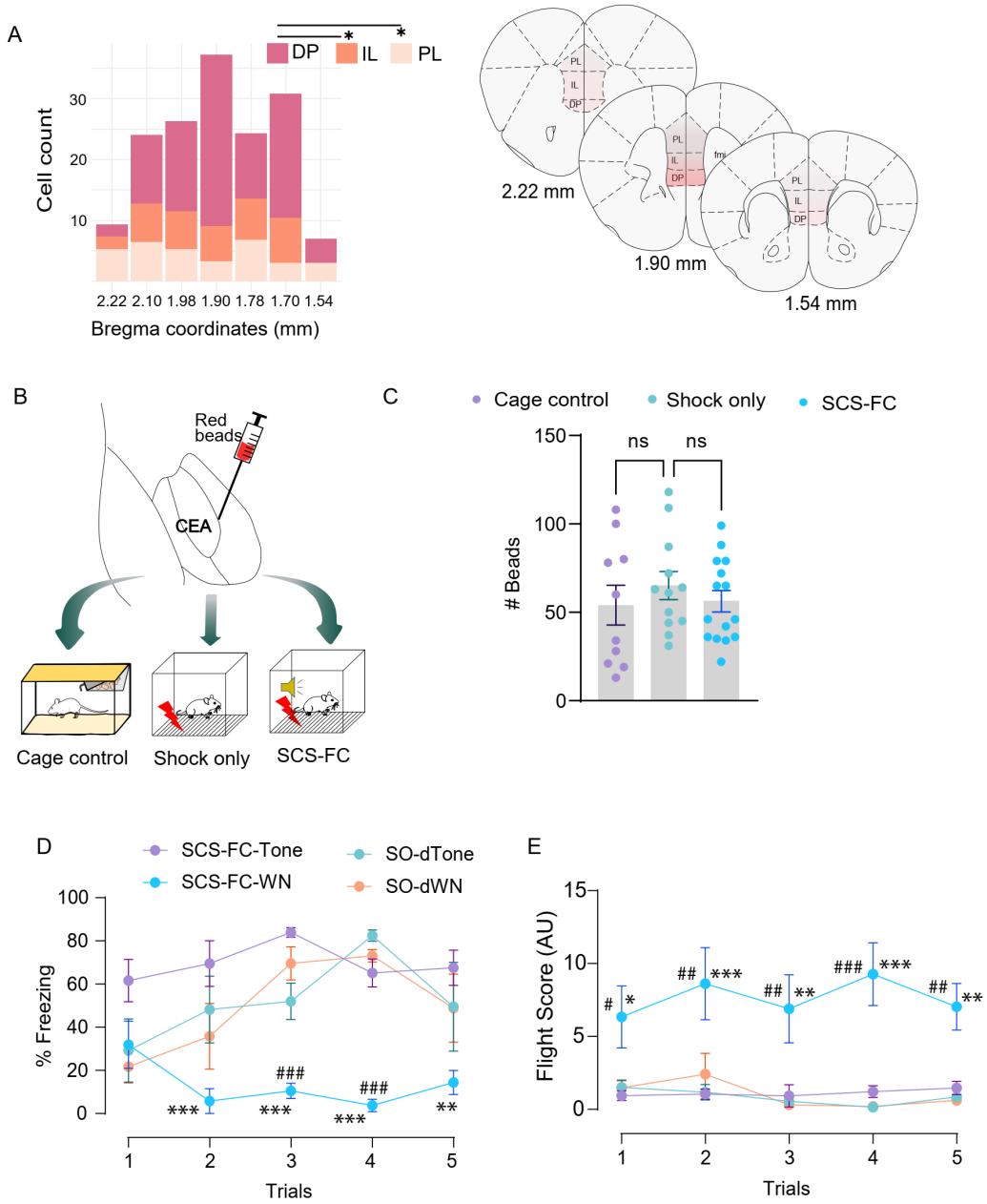

822

823 **Figure S1: Data related to Figure 1.**

824 **A**, Number of CeA-projecting mPFC cells across the antero-posterior axis (2.22 mm to 1.54

825 mm). One-way ANOVA, $F_{(2,15)} = 5.51$, $p = 0.016$, followed by Bonferroni's post-hoc test. *$p<0.05$.

826 **B**, Strategy used to study cFos activation in CeA-projecting DP cells.

827 **C**, Beads across groups (N = 6; 3-4 slices per group). One-way ANOVA, $F_{(2, 34)} = 0.4906$, $p =$

828 0.6165, Bonferroni's test, ns.

829 **D**, Freezing of cFos groups. For shock-only (SO) mice, freezing values are taken from the same

830 period of the session when the SCS would occur (SO-dTone or SO-dWN). Two-way ANOVA

831 (cue X trial, $F_{(12,60)} = 2.37$, $p<0.01$), followed by Bonferroni's post-hoc test.

832 **E**, Flight scores of cFos groups. For shock-only (SO) mice, flight scores are calculated from the

833 same period of the session when the SCS would occur (SO-dTone or SO-dWN). Two-way

834 ANOVA (cue X trial $F_{(12,48)} = 1.48$, $p>0.05$), followed by Bonferroni's post-hoc test. *P<0.05,

835 **P<0.01, ***P<0.001 vs SCS-FC-Tone; #P<0.05, ##P<0.01, ###P<0.001 vs SO-dWN.

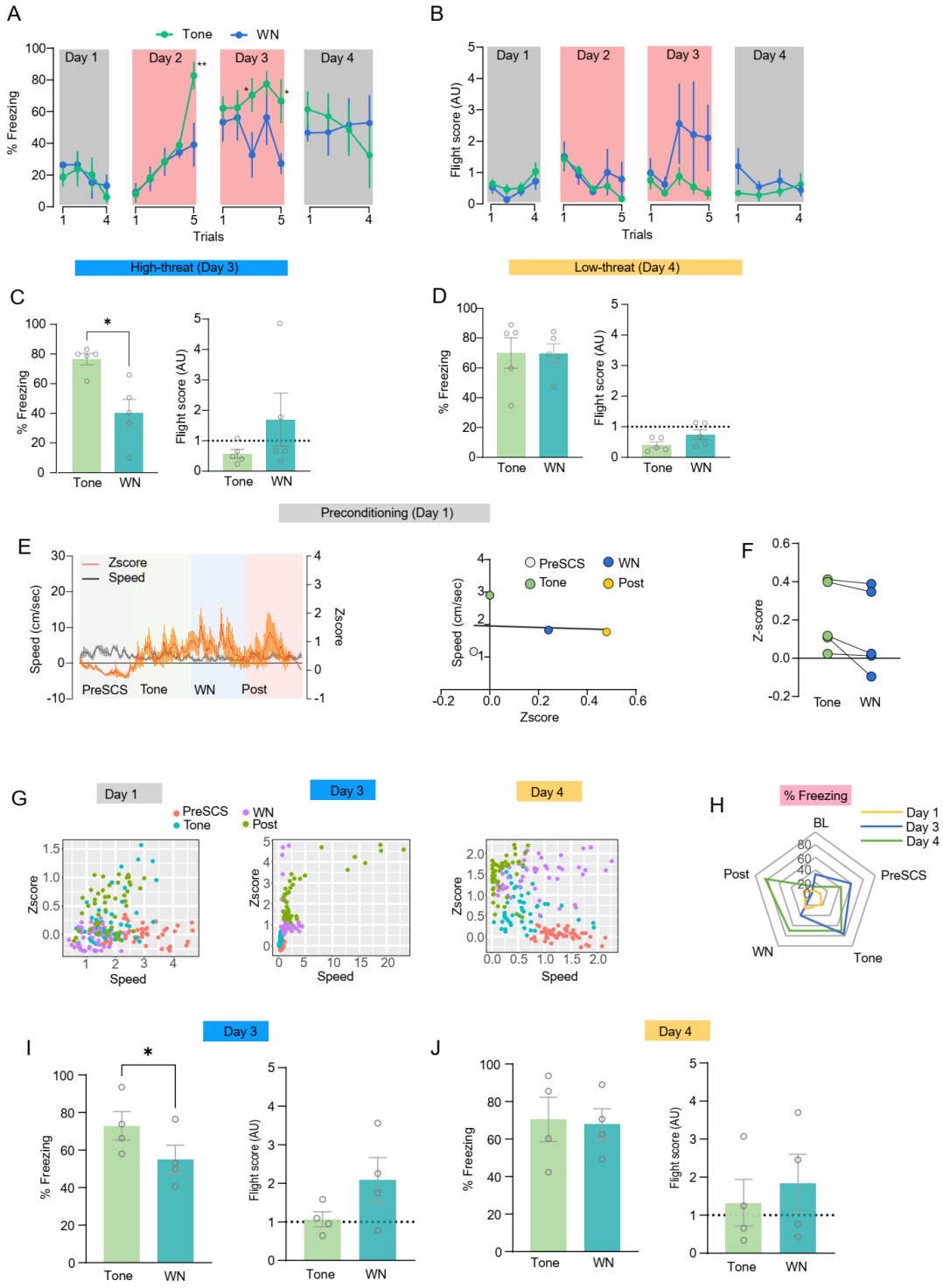

Figure S2: Data related to Figure 2.

838 **A**, Freezing of mice from calcium imaging experiments (N = 5). Two-way ANOVA, Trial x
839 Stimuli, $F_{(17,68)} = 2.36$, $p = 0.007$, Stimuli, $F_{(1, 4)} = 1.24$, $p = 0.327$, Trial, $F_{(17, 68)} = 5.79$, $p < 0.0001$
840 followed by Bonferroni's post-hoc test. * $p < 0.05$, ** $p < 0.01$.
841 **B**, Flight scores of mice from calcium imaging experiments (N = 5). Two-way ANOVA, Trial x
842 Stimuli, $F_{(17,68)} = 1.12$, $p = 0.35$, Stimuli $F_{(1, 4)} = 2.43$, $p = 0.194$, Trial, $F_{(17, 68)} = 1.35$, $p = 0.189$.
843 **C**, Average % freezing obtained from the mice subjected to the Ca^{2+} recordings during high-
844 threat (Day 3). Unpaired t-test, * $p < 0.05$ (N = 5).
845 **D**, Average flight scores obtained from the mice subjected to the Ca^{2+} recordings during high-
846 threat (Day 3). Unpaired t-test (N = 5).
847 **E**, *left*, Zscores of active neurons and speed in during preconditioning (N = 200 neurons). *Right,*
848 Correlation of Zscore (N = 200) with speed during preconditioning (Pearson correlation
849 coefficient, r = -0.079, $p = 0.9$).
850 **F**, Zscore of tone and WN of the entire DP-to-CeA population during preconditioning (paired
851 Student's t-test, n.s.).
852 **G**, Scatterplot of Zscore vs speed from preSCS, tone, WN and post-shock/cue (post) periods
853 from the last 3 trials of preconditioning (Day 1), high-threat (Day 3) and low-threat (Day 4)
854 sessions. Each dot represents averaged Zscore and speed over every 0.2 sec.
855 **H**, Spider plot of average % freezing from all the trials of preconditioning, high-threat (Day 3)
856 and low-threat (Day 4) sessions.
857 **I**, Freezing and flight scores from the no-lens control mice in the high-threat context (N = 4).
858 Unpaired Student's t-test, *$p < 0.05$.
859 **J**, Freezing and flight scores from the no-lens control mice in the low-threat context (N = 4).
860 Unpaired Student's t-test, n.s.

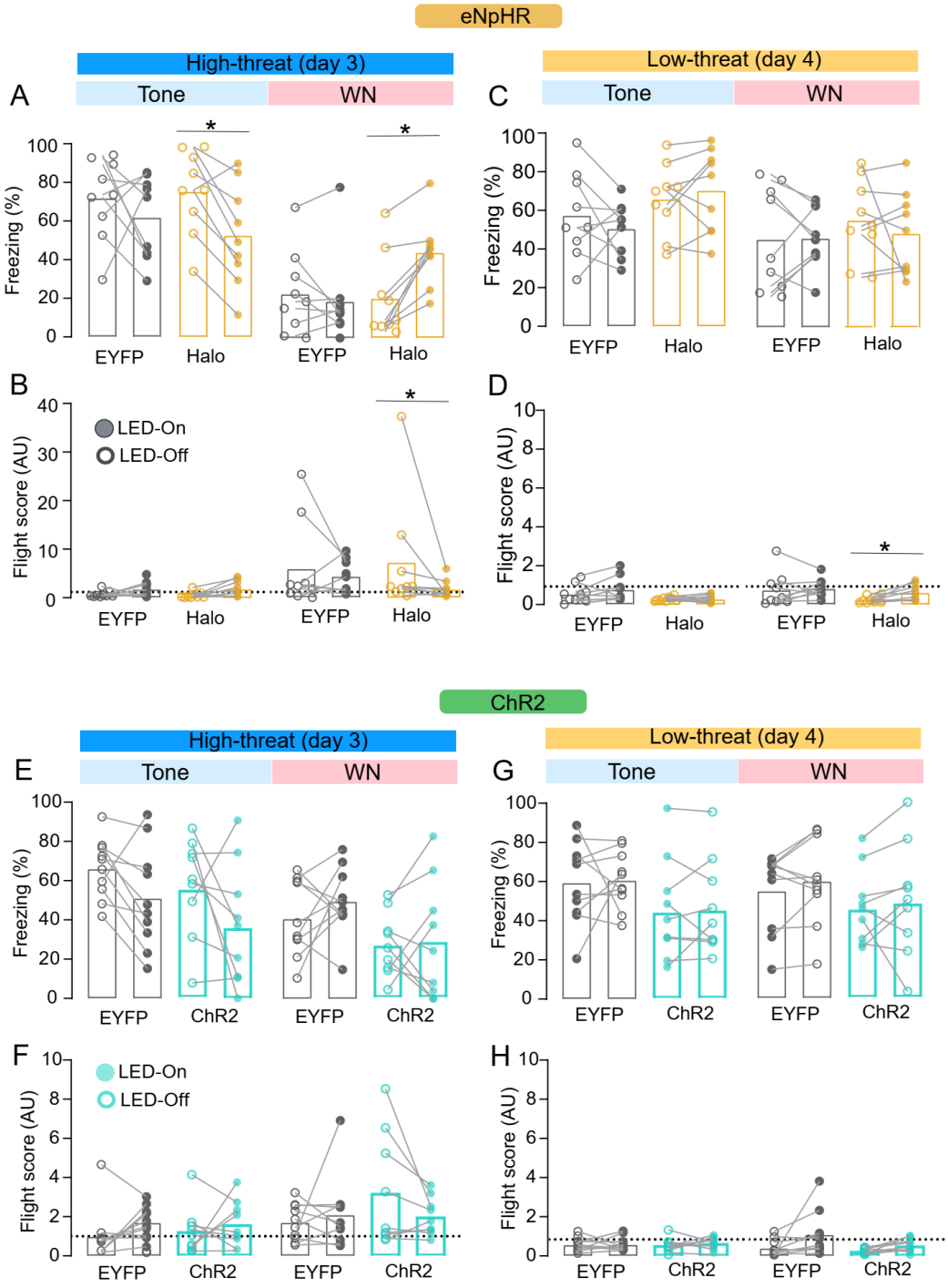

Figure S3: Data related figure 4

A, Effect of optogenetic inhibition in EYFP (N = 9) and eNpHR (N = 9) groups on freezing in the high-threat context (LED-on vs LED-off, Mann-Whitney, *P<0.05).

865 **B**, Effect of optogenetic inhibition in EYFP (N = 9) and eNpHR (N = 9) groups on flight in the
866 high-threat context (LED-on vs LED-off, Mann-Whitney, *P<0.05).

867 **C**, Effect of optogenetic inhibition in EYFP (N = 9) and eNpHR (N = 9) groups on freezing in the
868 low-threat context (LED-on vs LED-off, Mann-Whitney, n.s.)

869 **D**, Effect of optogenetic inhibition in EYFP (N = 9) and eNpHR (N = 9) groups on flight in the
870 low-threat context (LED-on vs LED-off, Mann-Whitney, n.s.)

871 **E**, Effect of optogenetic excitation in EYFP (N = 10) and ChR2 (N = 9) groups on freezing in the
872 high-threat context (LED-on vs LED-off, Mann-Whitney, n.s.).

873 **F**, Effect of optogenetic excitation in EYFP (N = 10) and ChR2 (N = 9) groups on flight in the
874 high-threat context (LED-on vs LED-off, Mann-Whitney, n.s.).

875 **G**, Effect of optogenetic excitation in EYFP (N = 10) and ChR2 (N = 9) groups on freezing in the
876 low-threat context (LED-on vs LED-off, Mann-Whitney, n.s.).

877 **H**, Effect of optogenetic excitation in EYFP (N = 10) and ChR2 (N = 9) groups on flight in the
878 low-threat context (LED-on vs LED-off, Mann-Whitney, n.s.).

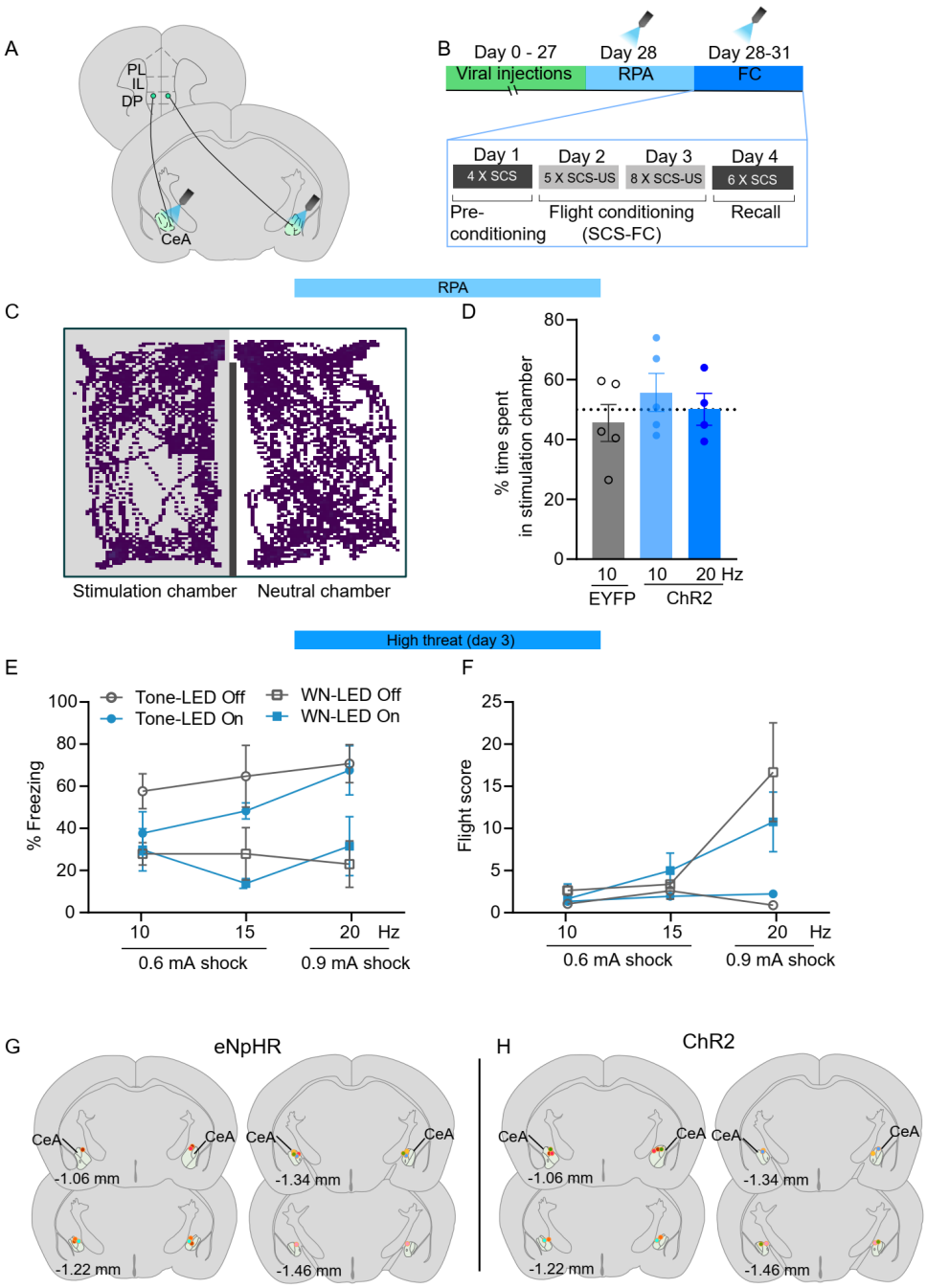

Figure S4: Data related to Figure 4.

A, Schematic of optogenetic terminal stimulation of DP-to-CeA neuronal projections.

B, Experimental timeline.

C, Representative activity plots in EYFP and ChR2 expressing mice.

884 **D**, % time in the stimulation chamber in EYFP (10 Hz, N = 5) and ChR2 (10 Hz, N = 5; 20 Hz, N
885 = 4) groups at different stimulation frequencies. One-way ANOVA ($F_{(2, 11)} = 0.73$, $p = 0.502$).
886 **E-F**, % freezing (E) and flight scores (F) to the tone and white noise (WN) following blue light
887 stimulation during day 3 at different stimulation frequencies and shock intensities (at 0.6 mA - 10
888 Hz, N = 9; 15 Hz, N = 3; at 0.9 mA - 20 Hz, N = 5). Two-way ANOVA (*for % freezing*,
889 Stimulation frequency x Shock intensity, $F_{(6, 56)} = 0.76$, $p = 0.601$, Stimulation frequency, $F_{(2, 56)} =$
890 1.10, $p = 0.339$, Shock intensity, $F_{(3, 56)} = 8.37$, $p = 0.0001$; *for flight*, Stimulation frequency x
891 Shock intensity, $F_{(6, 56)} = 4.42$, $p = 0.001$, Stimulation frequency, $F_{(2, 56)} = 12.4$, $p < 0.001$, Shock
892 intensity, $F_{(3, 56)} = 6.67$, $p < 0.001$), followed by Bonferroni's post hoc test (tone/WN ON vs OFF
893 non-significant).
894 **G**, Atlas of fibre placements over the CeA for the eNpHR group (N = 9)
895 **H**, Atlas of fibre placements over the CeA for the ChR2 group (N = 9)
896
897

A

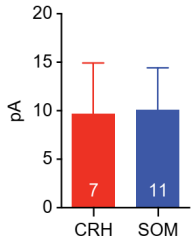

B

Firing Properties of DP-targeted CeA Neurons

DP-Excited cells (n=11)				
Classification	**Spike Threshold** (mV)	**Spike Latency** (ms)	**Spike Frequency Adaptation** (3rd ISI/Last ISI)	**Sag** (% steady-state)
Regular spiking (n=5)	-42 ± 2	46 ± 12	0.62 ± 0.11	17 ± 1
Bursting (n=4)	-43 ± 2	80 ± 40	–	21 ± 7
Late-firing (n=2)	-45 ± 6	194 ± 46	0.62 ± 0.04	11 ± 2

Figure S5: Data related to Figure 5.

A, The amplitude of disynaptic IPSCs evoked by ChR2 stimulation of DP terminals (Unpaired Student's t-test, $t_{(16)}$= 0.055; p = 0.96).

B, The firing properties of DP-targeted CeA neurons.